REPORT DOCUMENTATION PAGE

Form Approved
OMB No. 0704-0188

Public reporting burden for this collection of information is estimated to average 1 hour per response, including the time for reviewing instructions, searching existing data sources, gathering and maintaining the data needed, and completing and reviewing the collection of information. Send comments regarding this burden estimate or any other aspect of this collection of information, including suggestions for reducing this burden, to Washington Headquarters Services, Directorate for Information Operations and Reports, 1215 Jefferson Davis Highway, Suite 1204, Arlington, VA 22202-4302, and to the Office of Management and Budget, Paperwork Reduction Project (0704-0188), Washington, DC 20503.

1. AGENCY USE ONLY *(Leave blank)*

2. REPORT DATE
April 1992

3. REPORT TYPE AND DATES COVERED
Unclassified 1/90 to 3/91

4. TITLE AND SUBTITLE
Penetration Mechanics of Composites

5. FUNDING NUMBERS
DAAL03-89-K-0031

6. AUTHOR(S)
N.S. Brar, B. Azzi

7. PERFORMING ORGANIZATION NAME(S) AND ADDRESS(ES)
University of Dayton Research Institute
300 College Park
Dayton, Ohio 45469-0180

8. PERFORMING ORGANIZATION REPORT NUMBER

9. SPONSORING/MONITORING AGENCY NAME(S) AND ADDRESS(ES)
U. S. Army Research Office
P. O. Box 12211
Research Triangle Park, NC 27709-2211

10. SPONSORING/MONITORING AGENCY REPORT NUMBER
ARO 24102.3-MS

11. SUPPLEMENTARY NOTES
The view, opinions and/or findings contained in this report are those of the author(s) and should not be construed as an official Department of the Army position, policy, or decision, unless so designated by other documentation.

12a. DISTRIBUTION/AVAILABILITY STATEMENT
Approved for public release; distribution unlimited.

12b. DISTRIBUTION CODE

13. ABSTRACT *(Maximum 200 words)*

This report contains 3 sections: (1) the tensile strength of roving bundles of S-2 Glass® fibers (quasistatic strength of 535 ± 16 ksi) is measured using a modified split Hopkinson bar with two specimen designs at strain rates 10^3/s. The mean tensile strength measured from one sample design is ~700 ± 150 ksi at a strain rate of ~600 s^{-1}, and ~500 ± 120 ksi at a strain rate of ~1200 s^{-1} from the other. There is a very good agreement on the monofilament strength derived from the statistical analysis of the stress-strain data obtained from the two sample designs. (2) A reverse impact technique to measure the force on projectile noses penetrating fiber-reinforced plastic target panels is presented. 50 mm diameter GRP and KRP flyers are impacted against different nose-shaped steel bar targets instrumented with manganin gauges. The penetration into the 12.7 mm thick GRP is steady for the flat nose bar, but transient for the conical and hemispherical nose shapes. The penetration into the 37.4 mm thick KRP is steady for the conical and hemispherical nose shapes.

(Continued next page)

14. SUBJECT TERMS composites, fibers, tensile strength, strain rate, ballistics, force, deceleration, penetration modes, shock, cavity expansion, fiber stretching

15. NUMBER OF PAGES

16. PRICE CODE

17. SECURITY CLASSIFICATION OF REPORT	**18. SECURITY CLASSIFICATION OF THIS PAGE**	**19. SECURITY CLASSIFICATION OF ABSTRACT**	**20. LIMITATION OF ABSTRACT**
UNCLASSIFIED	UNCLASSIFIED	UNCLASSIFIED	UL

NSN 7540-01-280-5500

Standard Form 298 (Rev 2-89)
Prescribed by ANSI Std Z39-18
298-102

13. ABSTRACT (Continued)

(3) Five modes of failure (shock, double shear, single shear, cavity expansion, tensile stretching) of S-2 Glass composites during penetration with different nose-shaped projectiles are identified. The shock stage is especially dominant in flat nose-shape projectiles and a simple model is presented.

TABLE OF CONTENTS

TABLE OF CONTENTS
(Concluded)

Accession For

NTIS GRA&I ☑
DTIC TAB ☐
Unannounced ☐
Justification

By
Distribution/

Availability Codes

Dist	Avail and/or Special
A-1	

3

LIST OF FIGURES

LIST OF FIGURES
(Concluded)

LIST OF TABLES

FOREWARD

Dr. Stephan J. Bless was the principle investigator responsible for the conduct of this effort until his departure from the University in August 1991. In September 1991, Dr. Nachatter S. Brar and Dr. A.M. Rajendran completed the effort as co-principal investigators. Mr. Bechara Azzi provided invaluable assistance to Drs. Brar and Rajendran in completion of the technical analysis and documentation produced under this contract.

The principal investigators thank Dr. Kalaisam Iyer and Dr. Iqbal Ahmad, the technical monitors, for their technical guidance and direction during the performance of this contract.

Other reports and papers generated through this contract were:

S.J. Bless and D.R. Hartman, "Ballistic Penetration of S-2 Glass Laminates," paper presented at 21st Int'l. SAMPE Meeting, Atlantic City, NJ, September 1989.

S.J. Bless, D.R. Hartman, and M. Benyami, "Ballistic Penetration Mechanics of Glass-Reinforced Phenolic Composites," paper presented at 22nd Int'l. SAMPE Meeting, Boston, MA, November 1990.

S. Bless, M. Benyami, and D. Hartman, "Penetration Through Glass Reinforced Phenolic," 22nd SAMPE Technical Conference Proceedings, Boston, MA, November 1990.

M. Benyami, S.J. Bless, and D.J. Jurick, "Techniques to Study Penetration Through Glass Reinforced Phenolic," paper presented at the Aeroballistic Range Association, October 1990.

SUMMARY

This report summarizes the results of research performed on ARO Contract No. DAAL03-89-K-0031, on the Penetration Mechanics of Fiber Laminate Composites during the period from January 1990 to March 1991. The report is divided into three sections. Section 1 summarizes the high strain rate tensile properties of glass fibers. Sections 2 and 3 summarize the force measurements and deceleration of projectiles penetrating composite targets, respectively. These latter sections are based on conference papers that have been published in the course of progress in the same time period.

Section 1 is a summary of high strain rate tensile properties measurements of the reinforcing fibers. Testing of roving bundles of S-2 Glass® fibers was performed using a split Hopkinson bar at strain rates to 10^3 s^{-1}. Two specimen designs were used. We measured the mean dynamic tensile strength to be about 700 ksi with a standard deviation of 150 ksi from one design and about 500 ksi with a standard deviation of 120 ksi from the other. The disparity in the data is attributed to differences due to specimen gauge lengths and stress concentrations that are to some degree artifact of the specimen design. The manufacturer's measured quasistatic strength was about 535 ksi with a standard deviation of about 16 ksi.

Section 2 is based on the paper that was submitted to the 23rd International SAMPE Technical Conference, Kiamesha Lake, NY, October 1991. This section is a summary of the measurements of forces exerted on different nose-shaped (conical, hemispherical, and blunt) while penetrating GRP and KRP plates. 12.7 mm and 37.4 mm thick and 50 mm in diameter GRP and KRP plates were launched in a gun barrel using lexan sabots and caused to strike 7.6 mm diameter steel bar targets. The bars were instrumented with manganin stress gauges. The mass of the projectile package (sabot and flyer) was about 20 times that of the bar target. Consequently, the projectile did not slow down appreciably during penetration through the flyer plate and the penetration took place at practically constant velocity. The measured peak stress for flat, conical, or hemispherical nose shapes penetrating into a 12.7 mm thick GRP at strike velocities of 544 to 659 m/s was 11 to 14 kbar. Measured peak stress in the case of 12.7 mm thick KRP under the same conditions was 6 to 8 kbar. For 37.4 mm thick KRP flyer plates the peak stress was about 10.5 kbar at a strike velocity of 680 m/s for the cone and hemispherical nose shapes. For 37.4 mm thick KRP flyer plates, the penetration was steady state. The

penetration mechanisms of the conical and hemispherical nose shapes were drastically different from those of the blunt nose. The technique was validated by comparison to data given in Section 3.

Section 3 is based on the paper presented at the Comvat Vehicle Survivability Symposium, April 1991. The section begins with a summary of the measurement of projectile deceleration into GRP targets in ballistic experiments. Post-shot targets were sectioned and the sections examined visually in order to characterize the failure modes. Five penetration stages were identified this way. The first being the shock stage, especially dominant in flat nose projectiles, for which a simple model was presented. Other failure modes were stipulated but no rigorous models to describe these were advanced. In the discussion we present the possible application of data on tensile properties of fibers (Section 1) to the stretching stage in the penetration process.

SECTION 1

HIGH STRAIN RATE TENSILE TESTING OF S-2 GLASS® FIBERS

S-2 Glass® fiber roving bundles were tested with a split Hopkinson bar at strain rates to 10^3/s. The modulus determined from measured stress-strain curves was anomalously higher than the static value for roving bundles. The measured dynamic strength was scattered below and above the quasi-static value for roving bundles. The reduced strength of bundles at high rates is probably an artifact of the test fixture design. The quasi-static engineering strength measured with the same fixture design agreed, after a judicious correction within experimental error, with the quasi-static value of bundles. A statistical analysis based on fiber residual stress distribution was developed. The analysis to estimate the actual area of the specimen at peak load was applied to the quasi-static and with somewhat different interpretation to the dynamic tests on S-2 Glass® bundles to predict the tensile strength of S-2 Glass® monofilament.

1. INTRODUCTION

Fiber reinforced plastics (FRP) have been widely used as armor materials because of their light weight, high strength, good structural and ballistic performance, and the relative ease with which their properties can be custom processed. A large body of published and proprietary data on ballistic performance of FRP suggests that the relative content of resin and fibers, the type of fibers, weaving pattern, and curing process are crucial to the ballistic performance of FRP. Bless and Hartman have recently evaluated the ballistic performance of glass fiber reinforced plastic (S-2 Glass® GRP) panels against 50 caliber FSPs at velocities in the range of 500 to 3000 m/s[1]. They studied the effects of resin type, glass weight, number of plies, and areal density on the ballistic limit. Benyami et al. measured the deceleration of conical, hemispherical and blunt nose shape projectiles into S-2 Glass® GRP panels[2]. Other studies have investigated the effects of transverse strength and density on the penetration mechanism of thick GRP[3].

These data are useful for the development of empirical and numerical models for the penetration process. Micromechanics based modeling of penetration into FRP requires dynamic properties of these materials at strain rates characteristic of ballistic impact. One of the important dynamic properties in this context is the compressive and tensile strengths of the composites at high strain rates[4,5]. However, to model the deformation and failure processes of the FRP in a fundamental manner requires the high strain rate properties of the constituent materials, resin and fiber. The high strain rate data on epoxy or resin has been well documented. On the other hand, high strain rate data on different types of fibers (carbon, glass, Kevlar) is very scarce.

Tsai and Schulman[6] tested bundles of fibers of coated and uncoated S-Glass with gauge lengths of 1, 4, 10, 20 inches at quasi-static rates using a standard Instron machine. For uncoated fibers, stress-strain curves from 1-inch gauge length samples were convex with initial (elastic) modulus of 8.7×10^6 psi and ultimate tensile strength of about 310 to 350 ksi. For 20-inch gauge length samples, stress-strain curves were essentially linear with an initial elastic modulus of about 11.9×10^6 psi (37percent higher than that obtained with 1-inch samples) and approximately the same ultimate strength. For coated strands of fibers, the initial elastic modulus was about the same as for the uncoated fibers, but the ultimate strength and strain to failure were 50 percent higher compared to uncoated fibers.

Tsai and Schulman assumed that the fibers exhibited a statistical strength distribution and inferred the average strength of the filament from the tests on bundles. Assuming that the fibers behaved elastically to failure, they postulated that deviation from linearity in the stress-strain curve (quantified by the ratio of the secant modulus to the initial modulus) represents exactly the fraction of intact fibers just below peak load. The statistical analysis applied to the 1-inch specimen data produced a predicted value for the strength of the monofilament of 565 and 600 ksi for the uncoated and coated fibers, respectively. These values appear to be 16 to 20 percent lower than the value of the quasi-static strength of the S-2 Glass® monofilament (713 ksi) given in Figure 1.1.

Serensen and Strelyaev[7] in the Soviet Union developed a statistical analysis, remarkably similar to what was done by Tsai and Schulman[6], to predict the filament mean strength from tests on fiber bundles.

Armenakas et al.[8] conducted tests on (coated) single fibers of glass (of unknown pedigree) with specimen lengths ranging from 12.7 mm to 127 mm (0.5-5 inches), at strain rates ranging from 10^{-3}/s to 10^{-1}/s, in the temperature range of -60 to 150°F. They found that:

(1) The dependence of strength on strain rate was greatest near room temperature (70°F); at higher or lower temperature the dependence of strength on strain rate was not so marked. Around 70°F the strength

decreased by about 37 percent from about 205 ksi to about 130 ksi with increasing strain rate in the range 10^{-3} to 10^{-1}/s for a fixed 5-inch gauge length.

(2) The strength dependence on temperature was greater for lower strain rates for a fixed gauge length. For a strain rate of about 10^{-3}/s and a fixed gauge length of 5 inches, the strength increased from 160 ksi at -60°F to a peak value of about 205 ksi around 70°F (an increase of about 28 percent) and then decreased rapidly at higher temperatures where at about 150°F the strength attained a value of about 85 ksi (a decrease by about 59 percent from the peak). At the higher strain rate of about 10^{2}/s the strength increased from 150 ksi at -60°F to a peak of about 170 ksi near 70°F (a modest increase of about 13 percent); at about 150°F the strength dropped down to about 85 ksi (a decrease of about 50 percent from the peak).

(3) The strength decreased with an increasing gauge length from about 200 ksi corresponding to a gauge length of 0.5 inch to about 130 ksi corresponding to gauge length of 5 inches at a temperature near 70°F and strain rate of about 10^{-1}/s (a decrease of about 35 percent).

(4) The modulus was practically constant (about 12×10^{6} psi) in the temperature range -60 to 160°F and in the strain range of 10^{-3} to 10^{-1}/s.

Armenakas et al. fitted a statistical distribution of the Weibul form to their data and derived a relationship between the parameters of the distribution and strain rate. The statistical model then allowed them to predict strength with strain rate which were in good agreement with the experimental results.

The present study on S-2 Glass® fibers was undertaken to characterize the strain rate tensile behavior of these fibers at higher strain rates. We performed tests with a split Hopkinson bar (SHB) at strain rates of the order of 10^{2} to 10^{3}/s. Quasi-static tests at rates of the order of 10^{-4}/s were also performed. Two specimen designs with gauge lengths of about 5 and 8 mm were used in both the quasi-static and the SHB tests. All the tests were performed at ambient temperature (72°F). We carried out statistical analysis of the data, similar to that of Tsai and Schulman, to predict the strength of a monofilament from the measured specimen strength.

TABLE 1.1

Typical Properties of Slightly Impregnated S-2 Glass® Fiber and ASTM Test Designation

Property		ASTM No.
Density (lb/in^3)	0.089-0.090	C693
Sound speed (ft/s)	19,200	
Tensile strength (ksi)	530-620	D2343 (72°F)
Young's modulus (Msi)	12.5-13	D2343
Ultimate strain (%)	5.4-5.8	D2343

2. MATERIALS

The fibers were S-2 Glass®. These were supplied by Owens/Corning Fiberglas Corporation, Granville, Ohio in two forms: 463AA750 (750 yd/lb) roving tow and G150 (1500 yd/lb) roving bundles (strands). The roving tow had 20 roving bundles (of 1500 yd/lb), and each roving bundle had 204 filaments. The mean diameter of a filament measured at about 0.036 inches (about 9 μm). Typical properties of slightly impregnated S-2 Glass® fibers and the corresponding ASTM standard test designations are summarized in Table 1.1. The D2343 designation refers to impregnated strands which are typically 60 percent glass by weight (50 percent by volume). The resin contribution to strength in these strands is about 9 to 12 ksi. Figure 1.1 shows a tensile strength histogram and Weibul distribution of hollow virgin filaments based on 128 tests[9]. The monofilament mean tensile strength was measured at 713 ± 9.5 ksi with a variance of about 2 percent. The average tensile strength of 463AA750 roving tow that we actually tested was 534.7 ± 15.8 ksi, based on 30 tests[9].

3. EXPERIMENTAL TECHNIQUE

As with most high rate testing, wave reverberations (ringing) in the specimen is the most severe shortcoming. These wave reverberations induce stress gradients in the specimen proportional to the rate and this causes anomalous strain and modulus measurements.

A. The Split Hopkinson Bar

The split Hopkinson bar is generally used at strain rates of the order of 10^2 to 10^3/s. The split Hopkinson bar at the University of Dayton Research Institute consists of 0.5 inch diameter incident (108-inch long) and transmitting (72-inch long) bars made of Inconel (yield strength = 36 ksi at 72°F, Young's modulus = 29 $\times 10^6$ psi, longitudinal wave speed about 5 mm/µs). The bar is used for both compressive and tensile testing[10]. Figure 1.2 shows a schematic of the position-time diagram illustrating the wave propagation in a split Hopkinson bar operating in the tensile mode. In this mode, the two threaded ends of the test specimen are screwed into the threaded holes in the incident and transmitter bars. When using a normal dog bone specimen, a 0.5-inch long (equal to the gauge length of the specimen) cylindrical collar made of Inconel is placed around the test specimen with its ends in good contact with the incident and transmitter bars. A 1-d stress compression pulse, whose duration equals twice the transit time along the striker bar, is produced in the incident bar on impact with the striker bar. The collar around the specimen transmits the pulse, essentially unchanged and without disturbing the specimen, to the transmitter bar on the other end of the specimen. In our tests with fiber the use of such a collar was impossible, and the specimen fixture, itself of steel, having a comparable impedance to that of Inconel, provided for the role of the collar. At the free end of the transmitter bar the pulse reflects as a tensile pulse and propagates in the opposite direction with essentially the magnitude of the compression pulse until it reaches the specimen. The pulse is dissipated in straining the specimen and eventually failing it, with only the strength of the specimen transmitted across. The technique is essentially equivalent to applying a velocity boundary condition of magnitude equal to that of the incident velocity to one end of the specimen while the other end is stationary. The bar is instrumented with two strain gauges at 36 inches from the specimen. The strain ε and stress σ in the specimen were reduced from the transmitted (ε_t) and the reflected (ε_r) strain recorded by the two gauges on the incident and transmitter bars, respectively. The strain ε and the stress σ in the specimen can be reduced from the following equations

$$\varepsilon = \frac{-2C_b}{L_s} \int_0^t \varepsilon_r \, dt$$

$$\sigma = \frac{A_b}{A_s} E_b \varepsilon_t$$

where C_b is the longitudinal bar wave speed, L_s, A_s, E_b, A_b are the specimen gauge length, specimen area, Young's modulus of the bar, and bar cross-sectional area, respectively.

The bar drawback listed in Table 1.1 is the position to which the triggering mechanism is cocked. The actual distance by which the striker bar is pulled is obtained by subtracting the drawback from 12 inches. A drawback of 6 inches would correspond to an actual distance of 6 inches, a drawback of 7 inches would correspond to a distance of 5 inches, and so forth. Figure 1.3 shows the calibration curves of the force and striker bar velocity as a function of drawback. A drawback of 10 inches for example would correspond to a striker velocity of about 200 in/s and a force of about 2500 lbs.

B. Specimen Design

Two specimen fixtures were designed as shown in the photographs in Figure 1.4. These are subsequently referred to as types A and B. The fixtures material was stainless steel. Gauge lengths for type A and B specimens were about 5 and 8 mm, respectively. The two designs were intended to check that the measurements were truly material properties and not an artifact of a particular design. Specimen design A was spool type with the fibers wrapped around the spool ends; in type B the fibers were strung in a groove between the ends of the specimen. In almost all of the tests, strands were extracted from the roving tow. We adhered to very strict procedures to prevent damage to the fibers. In spite of these precautions, some accidental or occasional damage was incurred to the specimen. We believe that this slight damage was inconsequential to the test results. The ends of fibers were secured to the specimens by means of epoxy (Epoxi-Patch® 0151, shear strength of about 13 MPa (1.85 ksi) at 77°F). We exercised meticulous care that epoxy may not seep into the gauge section, and whenever this happened by accident the specimen did not fail there. As we progressed we varied the number of fibers in each specimen These are listed in parentheses in column 2 of Table 1.2.

4. RESULTS AND DISCUSSION

We performed 45 tests: 38 with the split Hopkinson bar at strain rates of the order of 10^2 to 10^3/s, and seven at a quasi-static rate of 10^{-4}/s. Forty-one tests were performed on roving strands extracted from 463AA750 roving tow, one test (test 45) on G150 single strands, and three tests (tests 8, 9, 12) on piano wire. A high-speed (Imacon) camera, at a framing rate of 10^5 frames/sec, was used in six tests (tests 16, 17, 18, 19, 20, and 21) to

TABLE 1.2

Summary of Results

(Numbers in parentheses indicate number of bundles used in a specimen.)

Test no.	Spec. type (No. bundles)	Draw back (in)	Strain rate (1/s)	Meas. strength, σ_b (ksi)	Meas. failure strain	Meas. secant modulus, E_s (Msi)	Pred. fraction intact fiber, F	Pred. fiber strength, σ_b/F (ksi)
2	A (352)	7	2400-3300	305	.11	5.5	.44	693
3	A (352)	7		384	.13	6.4	.51	753
6	A (352)	7	2600-3400	406	.08	9	.72	564
7	B (20)	9	620	247	.07	3.5	.28	875
13	A (640)	6		254		5.6	.45	564
14	B (40)	6		377	.055	6.8	.54	693
23	A (352)	--	static	212	.05	4.2	.34	625
24	B (40)	--	static	212	.07	3.0	.24	883
25	A (352)	9	840-1120	470	.045	9.5	.76	618
26	B (40)	10.5	480	690	.048	14.4		
27	A (184)	10	1300-1500	400	.045	7.3	.58	690
28	B (60)	10	620-700	620	.055	11.3	.90	689
30	B (60)	10	680	740	.057	13.0		
31	B (60)	10		880	.055	16.0		
32	B (60)	10		880	.074	11.9		
33	A (172)	10	1000-1400	410	.072	5.7	.46	891
34	B (60)	10	570-720	740	.052	14.2		
35	B (60)	10	570-720	540	.054	10	.8	675
36	A (40)	10	1300-1500	480	.06	8	.64	750
37	B (60)	10	320-600	460	.056	8.2	.66	697
38	A (44)	10	440-1040	560	.042	13.3		
39	A (20)	10		740				
40	A (40)	--	static	257	.07	3.7	.30	857
41	A (40)	--	static	249	.07	3.6	.29	857
42	B (60)	--	static	239	.066	3.6	.29	828
43	A (40)	--	static	213	.06	3.6	.29	734
44	A (40)	--	static	228	.065	3.5	.28	814
45	A (40)	10		420	.055	7.6	.61	688

observe the location of failure of the fibers along the gauge length of the specimen and also the mode of failure.

In Table 1.2 we list the actually measured specimen strength, which we shall interchangeably use to signify the bundle strength σ_b in the fifth column, the strain rate in the fourth column, the measured ultimate strain in the specimen in the sixth column, the measured secant modulus (the slope of stress-strain curve between zero and peak stress) in the seventh column, the predicted fraction F of intact fibers at peak load in the eighth column, and the predicted filament strength σ_f (σ_b/F) in the last column. The latter two quantities are introduced in Paragraph C and fully discussed there. The numbers in parentheses next to specimen type indicate the number of bundles in each specimen.

A. Quasi-static Test Results

We tested seven specimens at quasi-static rates of the order of 10^{-4}/s. Figure 1.5 shows the load-displacement curves produced in quasi-static tests with specimen A (test 44) and specimen B (test 42), respectively. The engineering strength results are given in column five of Table 1.2. The measured engineering strength averaged about 232 ksi and 226 ksi for types A and B, respectively, and therefore was in good agreement between the two specimens. There was no apparent relationship between the number of bundles per specimen and the measured strength. However, σ_b was about half that of the catalog (measured per ASTM2343). In the static tests with type A only half the sections failed, at which time the MTS machine was immediately shut off; the other sections were apparently undamaged. We can assume that only half of the sections supported the load. Accordingly, we believe the engineering strength should be increased by a factor of 2. There was, however, no such obvious correction for specimen B. In that particular specimen the fibers appeared to have failed at the grips at the ends of the gauge section, probably due to high stress concentration in these areas.

B. Dynamic Test Results

Figure 1.6 depicts the results from a rather typical test with the split Hopkinson bar (test 30). Figure 1.6 (a) shows the measured stress-strain curve and 1.6 (b) the stress or strain rate-time curves. As seen in Figure 1.6 (b) the strain rate is essentially constant after a ramp up period then decreases monotonously as the stress increases up to the peak. The average strain rate listed in Table 1.2 was derived as illustrated in Figure 1.6 (b). Figures 1.7 (a) and 1.7 (b) depict stress-strain curves showing the effect of strain rate on strength. Considering the scatter of data that is typical of Hopkinson bar testing, no such effect was conspicuous. Figures 1.8 (a) and 1.8 (b) are plots of the stress-strain curves obtained for approximately the same strain rate. The scatter in the data was typical of the scatter common to Hopkinson bar data; although, the scatter produced with type A was greater than that in type B. Figure 1.9 is a plot of the stress-strain rate obtained with specimen type B with the same striker velocity. It is shown that the scatter is within reasonable experimental error. Again, the scatter was greater for type A.

The test results are documented in Table 1.2. It is noteworthy to digress on the results of 10-inch drawback tests since these were by and large the most extensive. In these tests it is shown that the average strain for type A was about 1333 s^{-1} (tests 27, 33, and 36), double that for type B of about 658 s^{-1} (tests 28, 30, 34, and 35). We do not fully understand the reason for this difference in strain rates (it might be due to the difference in gauge lengths between the two specimen types). The average measured strength was 430 ksi for type A (tests 27, 33, and 36) and 660 ksi for type B (tests 28, 30, 34, and 35), or about 50 percent higher than that of type A.

In tests 37, 38, and 39 we ramped the loading pulse by putting a 0.5-inch diameter, 0.25-inch thick lexan disk between the striker bar and the transmitter bar. The ultimate strains we measured in these tests are extremely low. The reason being that having ramped the pulse we increased its width from 300 μs to 392 μs; the compressive wave reflected from the specimen and superimposed on the trailing edge of the tensile wave (reflected from the free end of the incident bar), which had not entirely cleared the gauge. In fact, for about 32 μs in the beginning, the gauge records the superposition of these waves and therefore the strain in the specimen is irreducible. The strength, however, should be valid since it is reduced from the other gauge. This can be seen in test 39, where the measured strength is about 740 ksi, and the measured strain is too low at about 3 percent. In order to circumvent this, the allowable pulse width must not exceed 360 μs. For this reason, the thickness of the lexan disk must be about half of that used, but we did not pursue this further.

We experimented with pretensioning the specimen by using a wedge that was designed to displace the specimen (type A only) by a maximum of 0.5 mm. In test 45, the only test with G50 strands, such a wedge was used. We measure a strength of about 210 ksi, and an estimated ultimate strain of about 3 percent, based on a gauge length of about 8 mm. The reason for these low measurements, we believe, is the residual stress induced by pretensioning. Assuming that a wedge displacement of about 0.25 mm was imposed on the specimen, then it was strained by 0.25/(8-0.25) = 3 percent, and assuming a linear stress-strain relationship, then at about 3 percent the stress is about 210 ksi (inferred from the measured stress-strain curve). The actual stress and strain in the specimen are then $2 \times 210 = 420$ ksi and $2 \times 0.03 = 0.06$, respectively.

Subsequently, we present a method for inferring the strength of a single fiber from the tests on bundles of fibers. The method, based on slack distribution of fibers, is analogous to that in reference [2], which was based on distribution of strength of fibers.

C. Statistical Analysis

The following analysis is based on the thesis that the fibers, especially those at the core of the bundle, initially have slack that leads to progressive failure rather than simultaneous failure of all the fibers, that this manifests itself in nonlinear (concave) stress-strain curves yielding low modulus. A fiber slack distribution based probabilistic analysis aims at inferring the single fiber strength from tests on bundles.

Let $f(\varepsilon)$ be the probability density function representing the slack distribution in the fibers. Then $F(\varepsilon)$ the cumulative probability function represents the fraction of the number of fibers with slack $\varepsilon_0 \leq \varepsilon$. $F(\varepsilon)$ is by definition

$$F(\varepsilon) = \int_{-\infty}^{\varepsilon} f(x)dx$$

Let N be the number of fibers present in a specimen, A the area of the specimen, A_1 the area of a single fiber, and E_1 the modulus of a single fiber. Then the average stress in the bundle at a strain ε is approximated by

$$\sigma_b(\varepsilon) \approx \frac{1}{A} \sum_x N \frac{\partial F(x)}{\partial x} \Delta x (\varepsilon - x) E_1 A_1$$

or given exactly by

$$\sigma_b(\varepsilon) \approx \frac{1}{A} \int_0^{\varepsilon} N \frac{\partial F(x)}{\partial x} (\varepsilon - x) E_1 A_1 dx$$

Using $NA_1 = A$, we derive the slope of the stress-strain curve at ε

$$\frac{d\sigma_b}{d\varepsilon} = \frac{\partial}{\partial \varepsilon} \int_0^{\varepsilon} \frac{\partial F}{\partial x} (\varepsilon - x) E_1 dx$$

It can be shown that the differentiation of the integral leads to

$$\frac{d\sigma}{d\varepsilon} = F(\varepsilon)E_1$$

Then F(ε) is given by

$$F(\varepsilon) = \frac{\frac{\partial\sigma_b}{\partial\varepsilon}}{E_1}$$

And the monofilament strength is given by

$$\sigma_f = \frac{\sigma_b}{F(\varepsilon)}$$

The last two equations are very important. The first provides us with the fraction of the number of fibers supporting the peak load and the second allows us to predict the monofilament strength by correcting the actually measured specimen engineering strength. It should be observed that unlike the results in references [1, 2, and 3], F is independent of the form of the probability density function. Technically one should derive F(ε) from the average slope of the straight line segment of the stress-strain curve, and use E_1, the elastic modulus of the monofilament, at the rate the test is conducted. Cagnoux[11], in his thesis, presented data on shock loaded pyrex glass (strain rate 10^5 s^{-1}). The measured initial elastic modulus from these data was about 75 GPa. This was within 1 percent of the modulus typically measured in an acoustic test, which is typical of strain rates of the order of 1 s^{-1} or less. Since there is no evidence that the modulus of bulk glass at these rates differs from the static values, we approximated E_1 by its static value. The tangent slopes of our σ-ε curves were highly variable. We believe this was due to sample ringing so we approximated $\partial\sigma_b/\partial\varepsilon$ by the slope of the secant between zero and peak stress. Specifically, we use for E_1 the value 12.5 Msi, the Young's modulus for impregnated strands (per ASTM D2343).

Details of applying the analysis to the static and dynamic tests are discussed in the next two sections. Results of the predictions are given in the last two columns of Table 1.2.

(1) Static Tests

We performed seven static tests with an MTS machine. A load-displacement (stress-strain) curve from a static test is shown in Figure 1.5. The curve is initially concave and slightly convex near the peak. The slope $\partial\sigma/\partial\varepsilon \leq 12.5$ along the curve. Tests 23, 40, 41, 43, and 44 were with type A, and tests 24 and 42 with type B. The measured secant modulus was about 3 to 4 x 10^6 psi, the measured peak stress (peak load divided by the original area) was about 212 to 257 ksi, the measured bundle ultimate strain was about 5 to 7 percent. Applying the analysis, the predicted fraction was 0.29 to 0.54 and the predicted monofilament strength was 625 to 857 ksi. These results are given in Table 1.2.

(2) Dynamic Tests

A stress-strain curve from a dynamic test under typical conditions is shown in Figure 1.6. The curve is initially concave-like in the static tests, but then intermediately it has a very high slope, substantially higher (1.5 to 5 times more) than the static handbook value of 12.5 Msi for slightly impregnated specimens.. The analysis was applied with $\partial\sigma/\partial\varepsilon$ set equal to the slope of the stress-strain curve between zero and peak stress levels. (Some curves had a double peak feature, with low strength, and these we analyzed up to the first peak.) It is worthwhile to elaborate on the 10-inch drawback tests (14 tests). The measured (bundle) strength, measured ultimate strain, measured secant slope, were respectively in the range 540 to 740 ksi, 5.2 to 7.4 percent, and, and 8.2 to 16 x 10^6 psi, for type B, and 400 to 740 ksi, 4.2 to 7.2 percent, and 5.7 to 13.3 x 10^6 for type A. The predicted F value and predicted monofilament strength σ_f were respectively in the range 0.66 to 1.33, 675 to 880 ksi (for $F \geq 1$, $\sigma_f \equiv \sigma_b$) for type B, and 0.46 to 0.64, 688 to 841 ksi for type A. These results are summarized in Table 1.2. The agreement between the predicted monofilament strength from the two specimen types was excellent.

5. CONCLUSIONS

We tested S-2 Glass® fiber at high tensile strain rates to 10^3 s^{-1} using a split Hopkinson bar and two specially designed specimens. Results with specimen A at quasi-static rate of the order of 10^{-4}/s agreed, after judicious correction, with the value for the manufacturer's static strength of the single bundle to within experimental error, but the specimen was found to fail invariably at only half the sections. There appeared to be no real effect of the number of bundles tested on the measured engineering strength.

The following conclusions can be drawn from the limited testing we performed with the split Hopkinson bar:

(1) Apparent dynamic modulus of glass fibers at strain rates of 10^2 to 10^3/s was a factor of 1.5 to 5 times the static value reported by the manufacturer for a single roving bundle. It could be that the measured ultimate strain is irreducible without alteration of the current technique.

(2) The measured bundle strength produced with type A specimens was about only half that of type B; the strength measured in type B was of the order of magnitude of the static strength of the filament.

(3) The strain rate measured in type A was about double that of type B, which might be attributed to the differences in gauge lengths.

(4) We can predict monofilament strength by probabilistic inference, independent of the form of probability density function, and there is a good agreement from the two specimen types for the strain rates considered.

(5) In the range we tested there was no real discernible dependence of strength on strain rate.

We recommend that testing be done that spans the full range of the MTS machines and beyond, with a range of specimen length; then perform the testing with the Hopkinson bar matching the upper limit of rate achievable with the MTS machine and progress to higher rates.

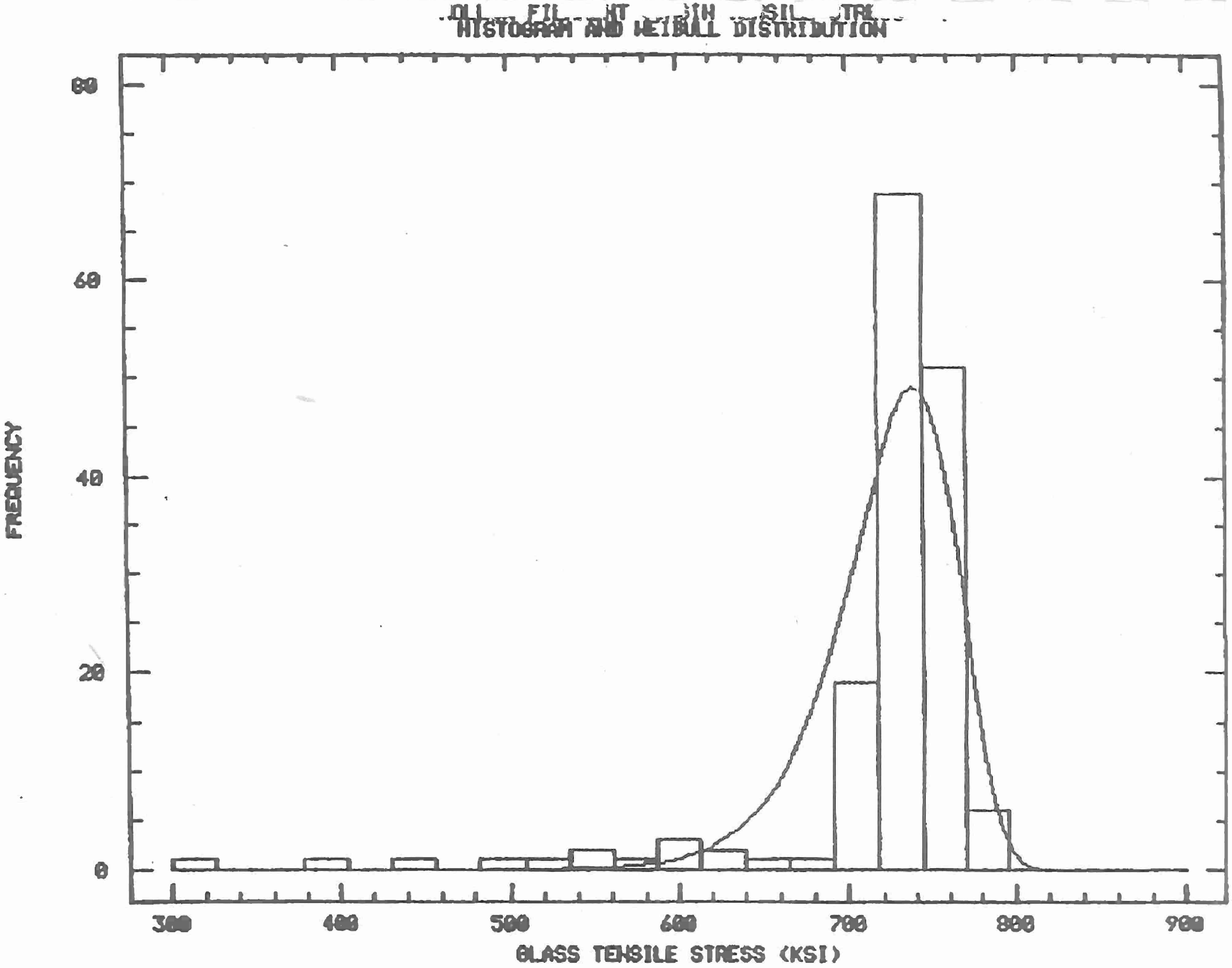

Figure 1.1 Histogram and Weibul distribution for tensile strength of hollow virgin filaments, based on 128 tests (source: Owens/Corning Fiberglas Corp.).

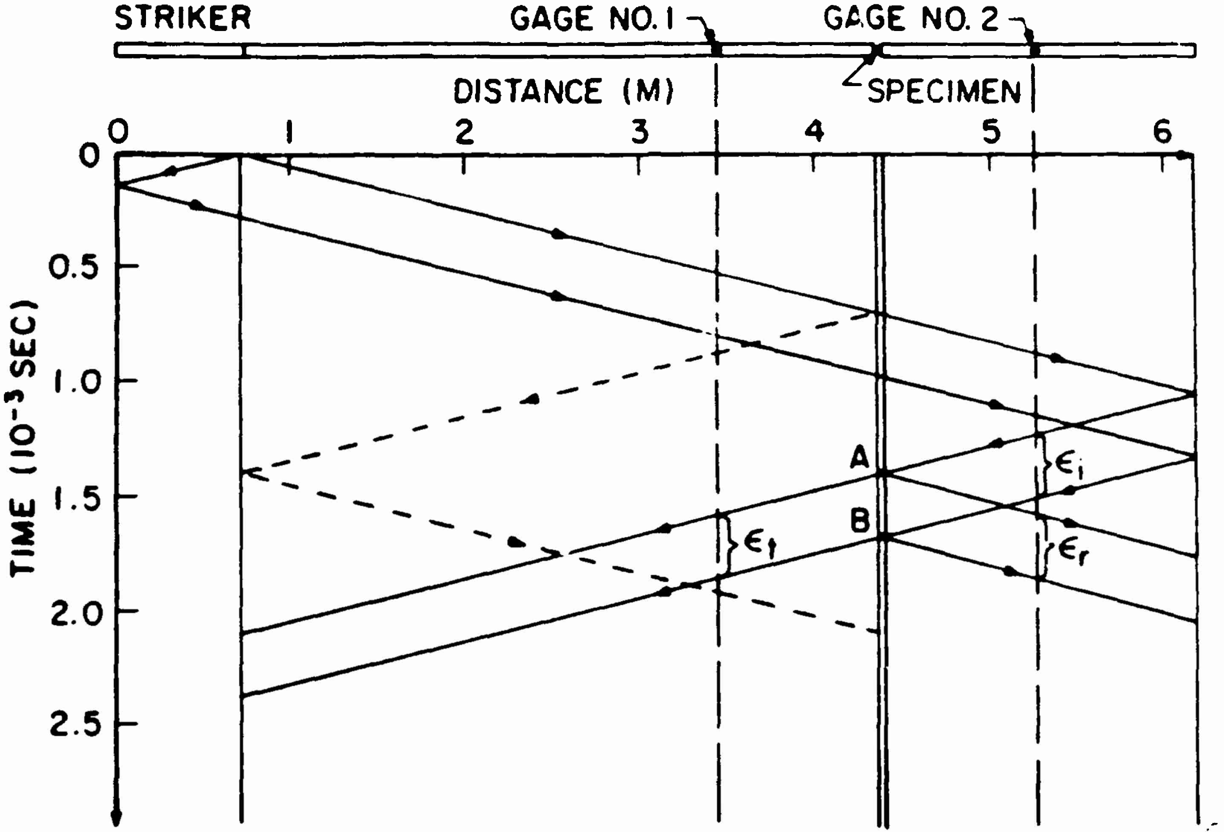

Figure 1.2. Schematic of split Hopkinson bar and x-t diagram illustrating wave propagation in the tensile mode (Reference 10).

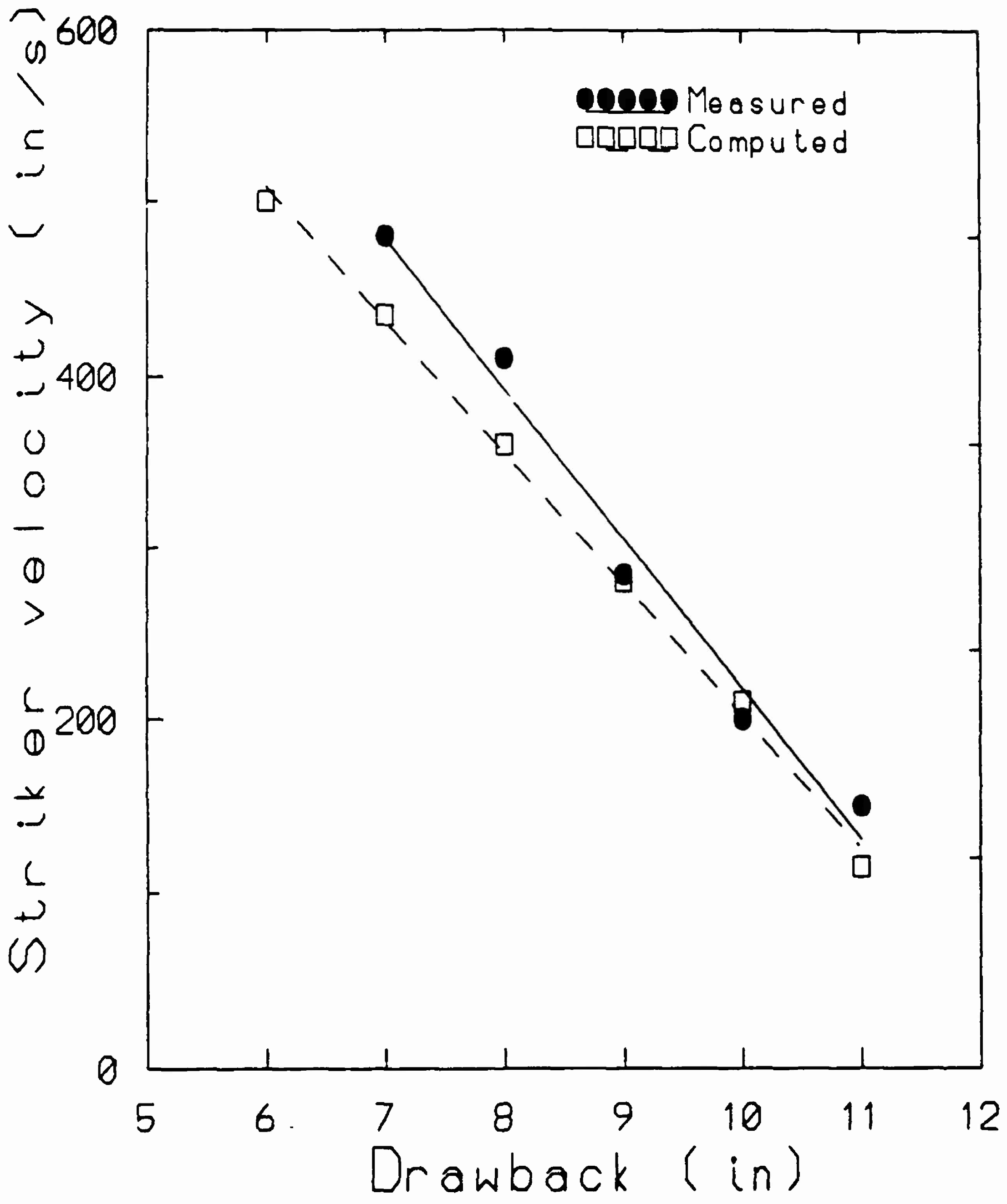

Figure 1.3. (a) Calibration curves for split Hopkinson bar: striker velocity versus drawback.

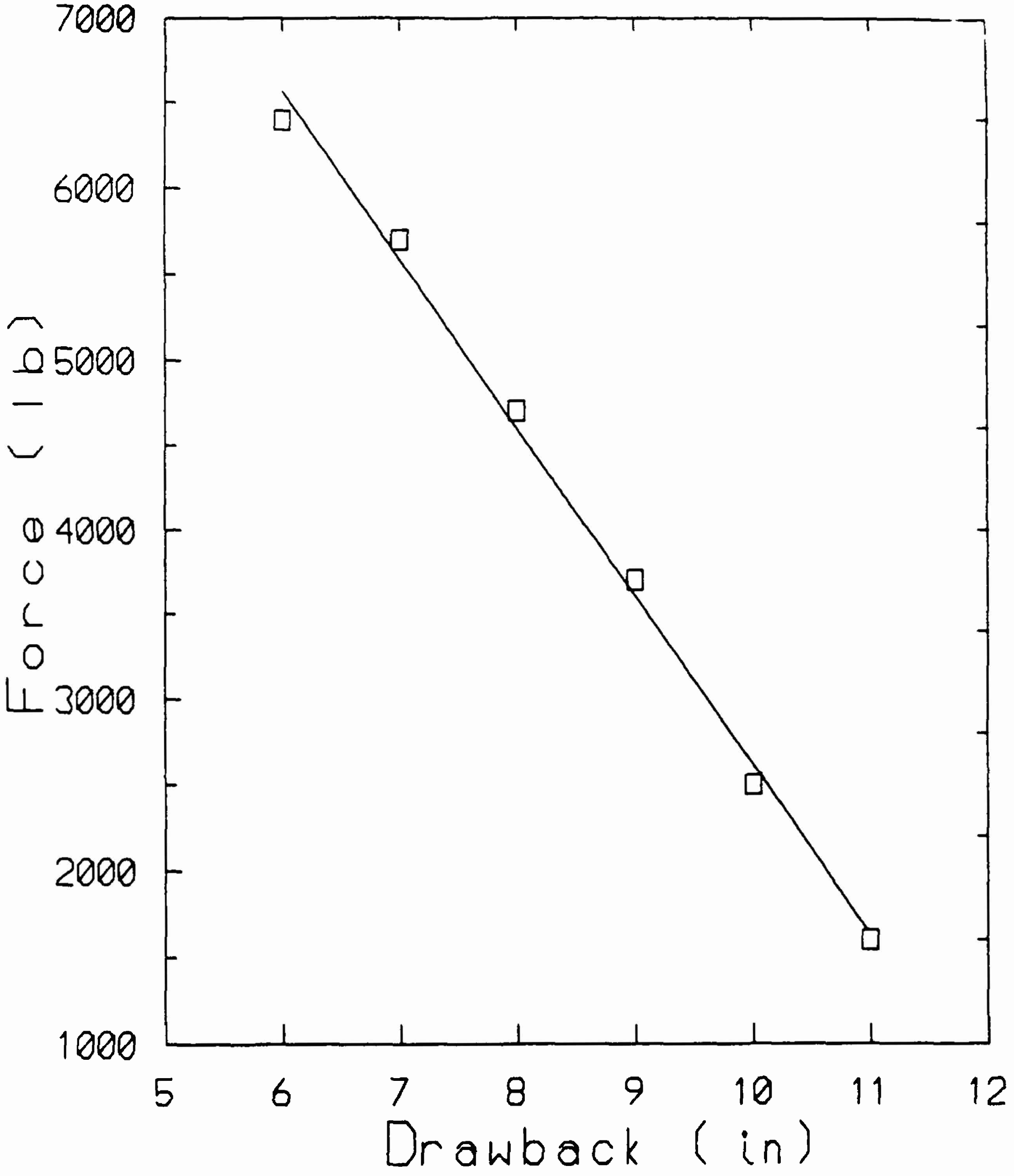

Figure 1.3. (b) Calibration curves for split Hopkinson bar: force versus drawback.

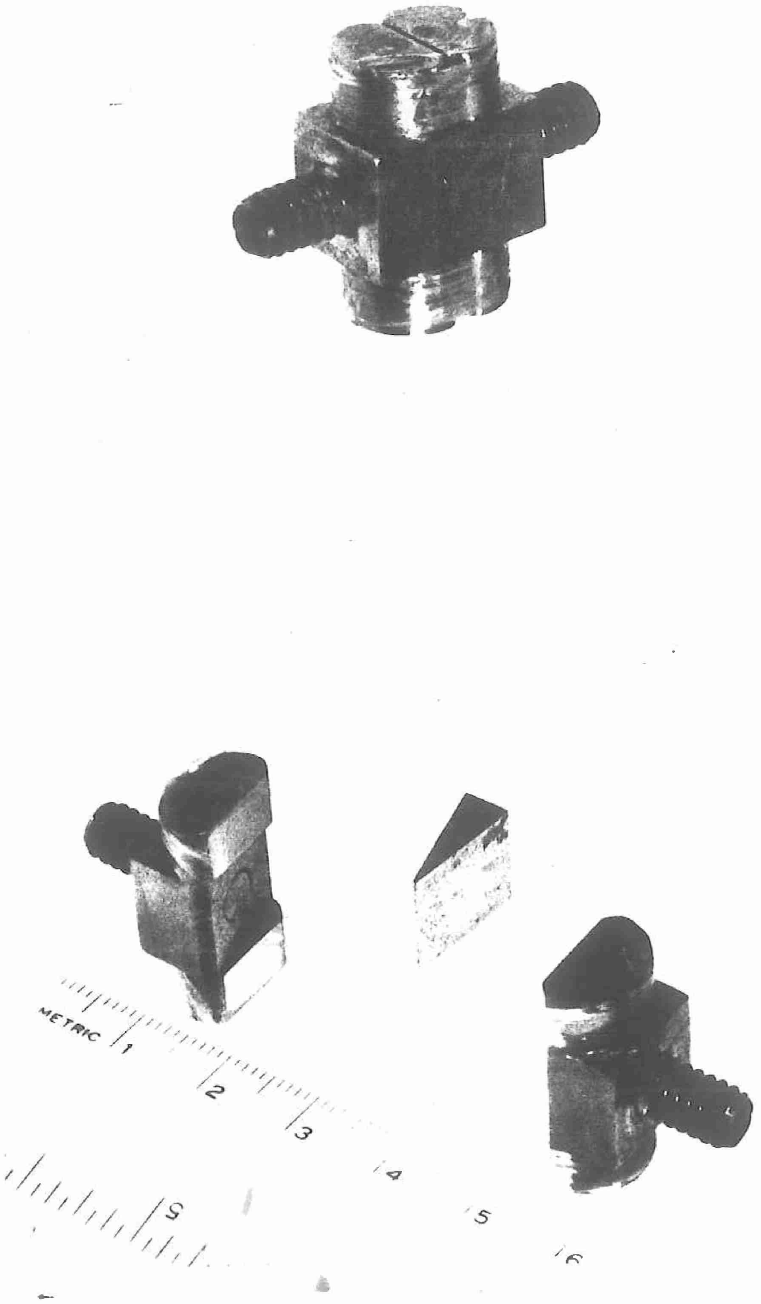

Figure 1.4. (a) Photographs of specimen design Type A (with a wedge) showing the fiber failure after test.

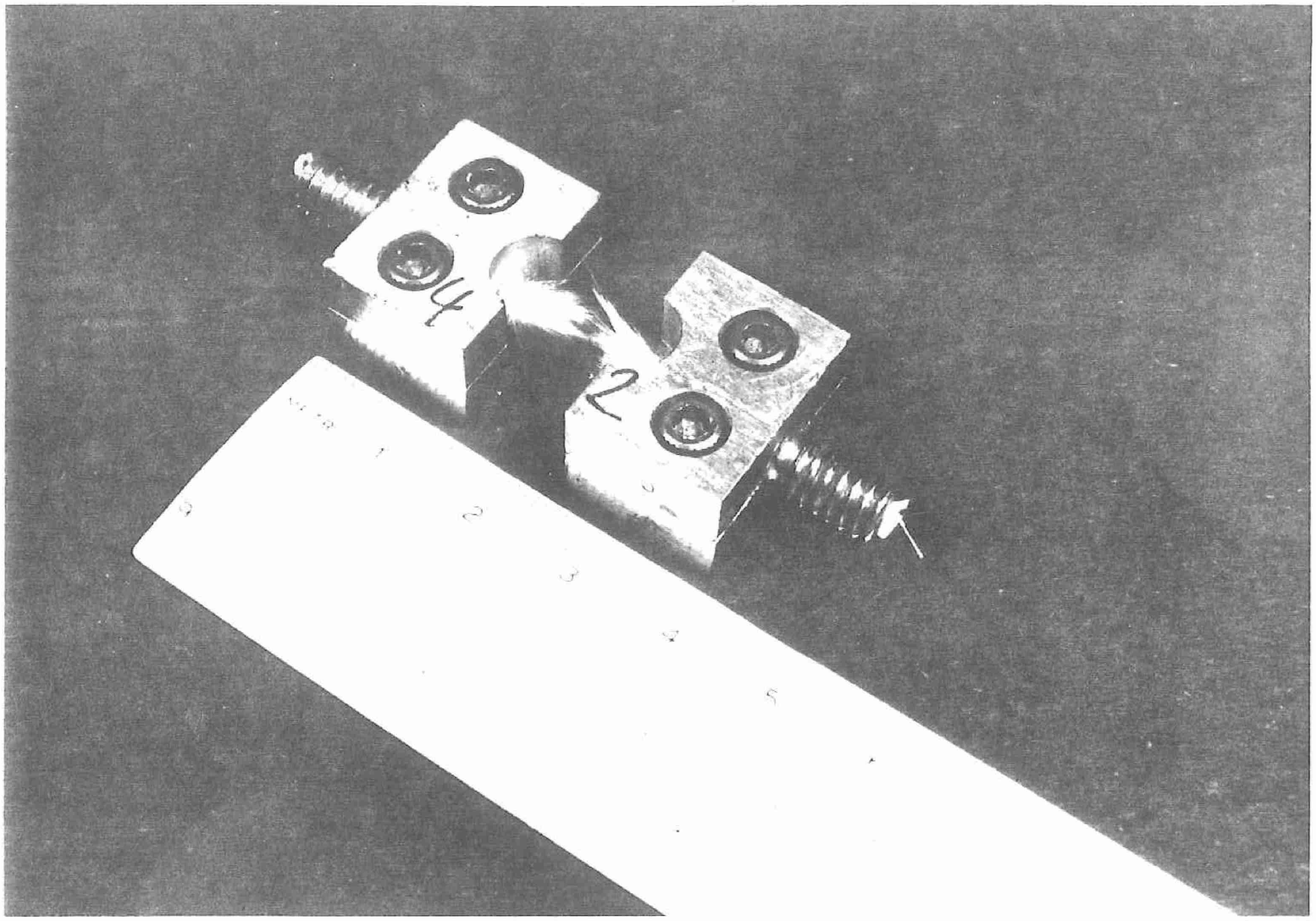

Figure 1.4. (b) Photograph of specimen design Type B showing the fiber failure after test.

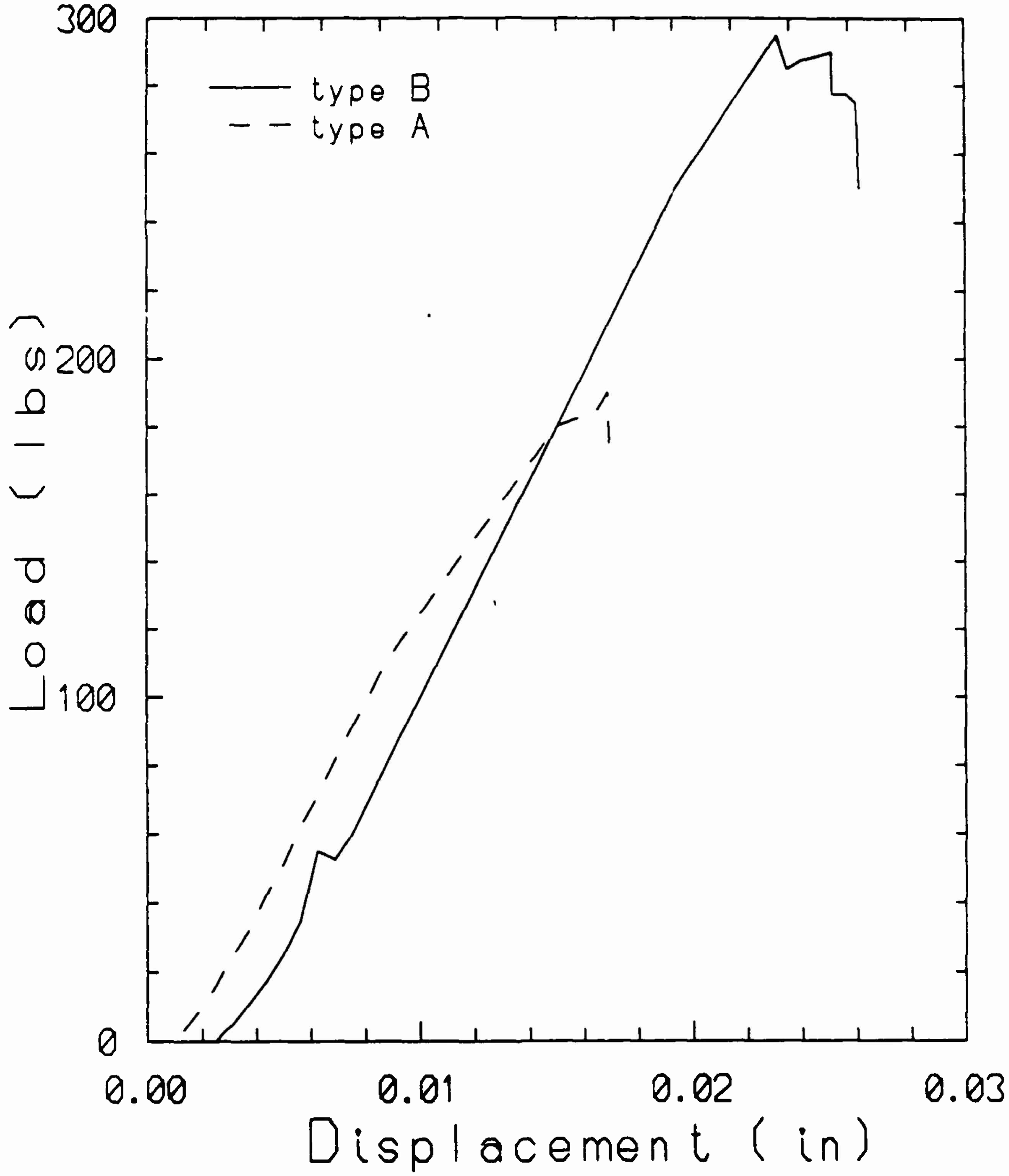

Figure 1.5. Load displacement curve for a typical quasistatic test with MTS machine with specimen Type A (Test 44) and Type B (Test 42).

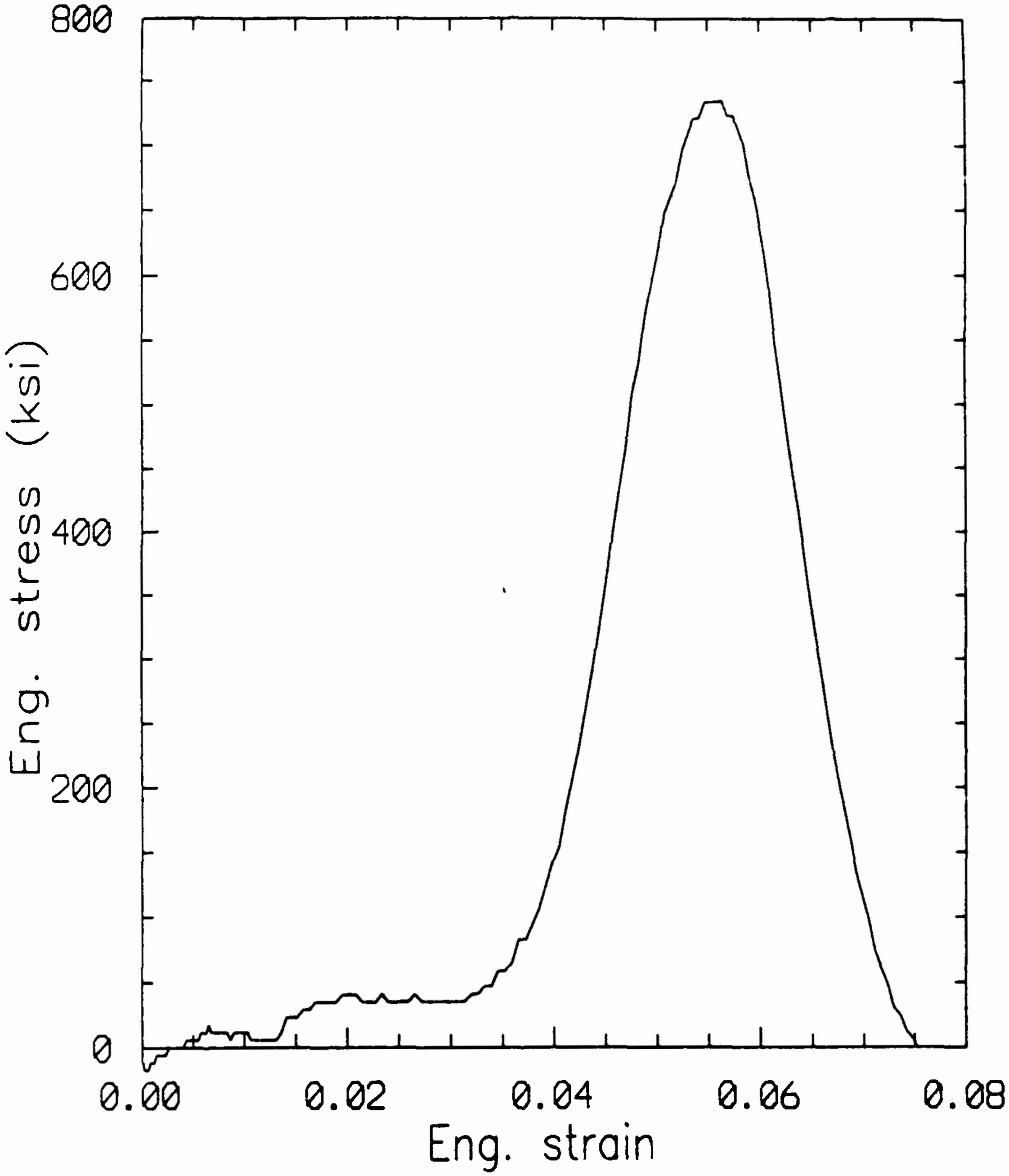

Figure 1.6. (a) Results from typical dynamic test with split Hopkinson bar (Test 30); stress-strain.

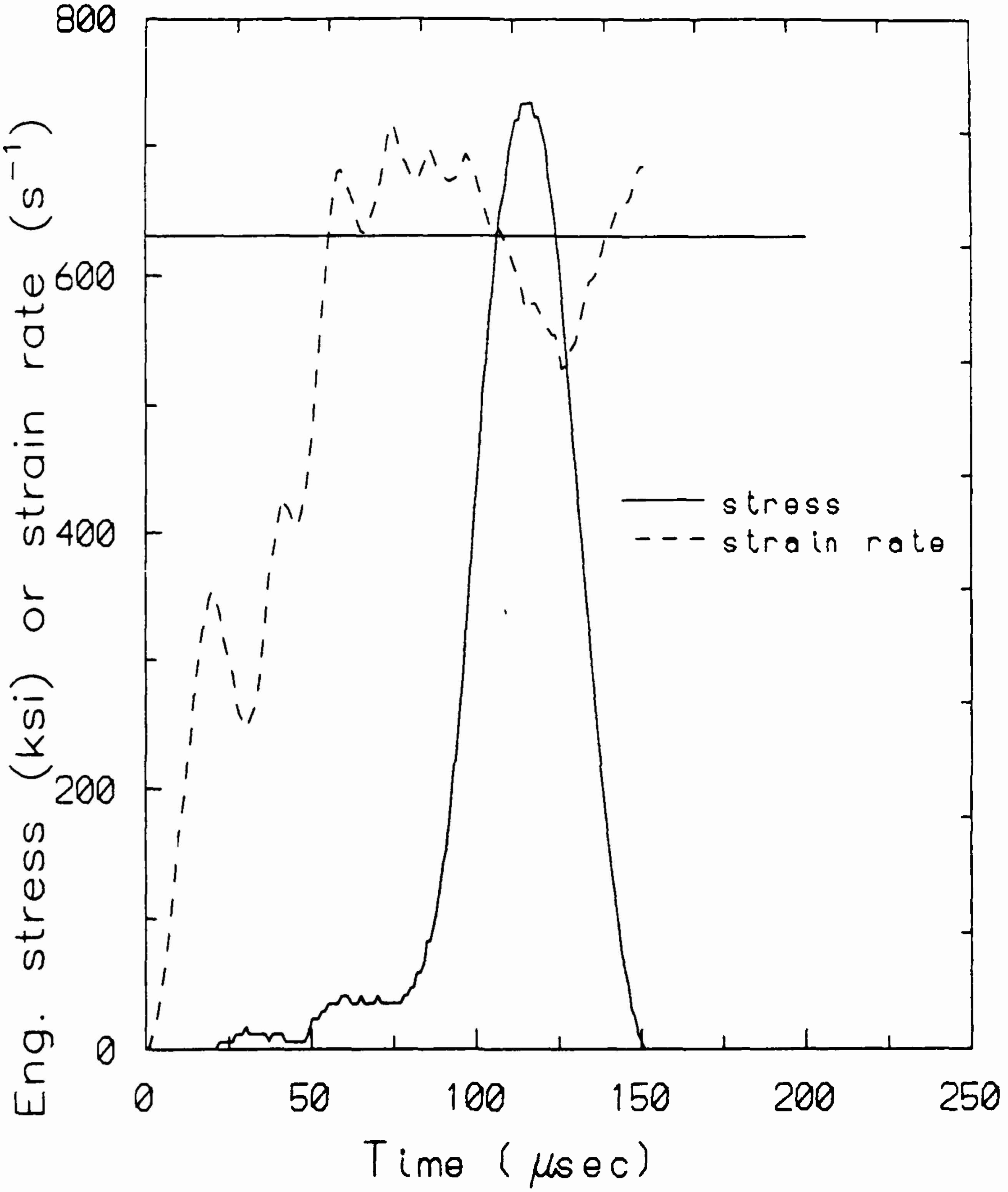

Figure 1.6. (b) Results from typical dynamic test with split Hopkinson bar (Test 30); stress time and strain rate-time.

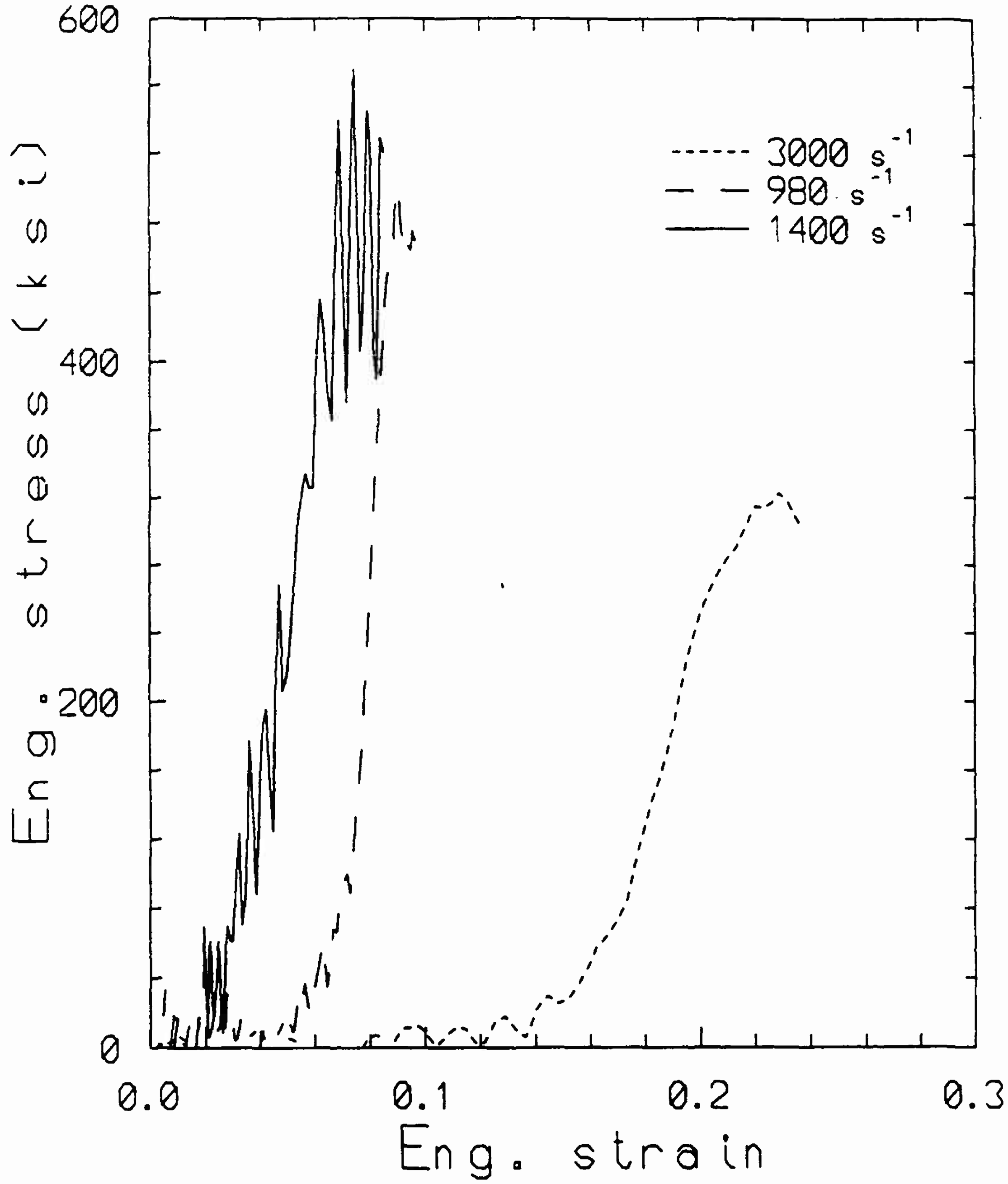

Figure 1.7. (a) Stress-strain curves showing the effect of strain rate; specimen Type A (Tests 6, 25, and 36).

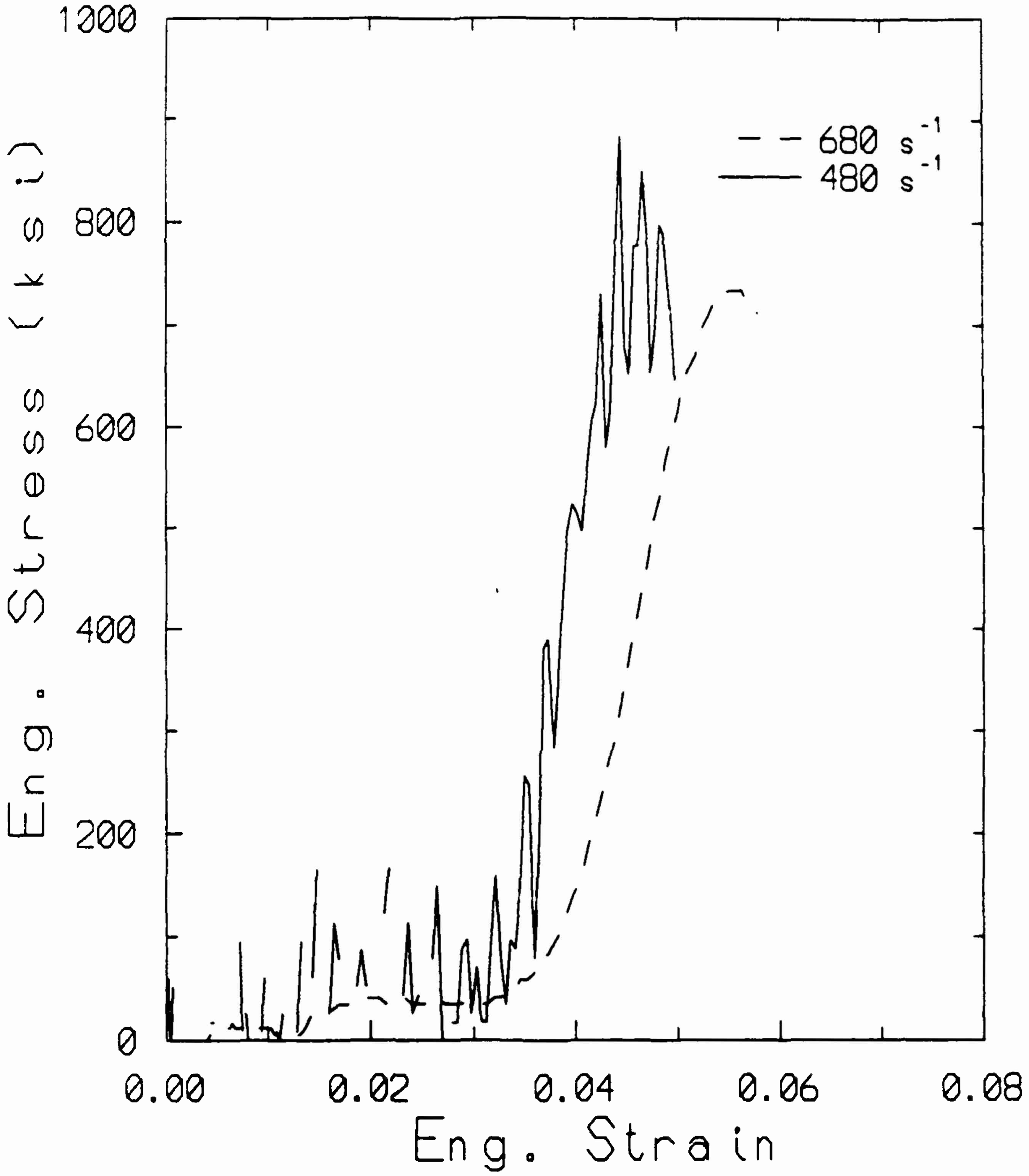

Figure 1.7. (b) Stress-strain curves showing the effect of strain rate; specimen Type B (Tests 7, 14, 26, and 30).

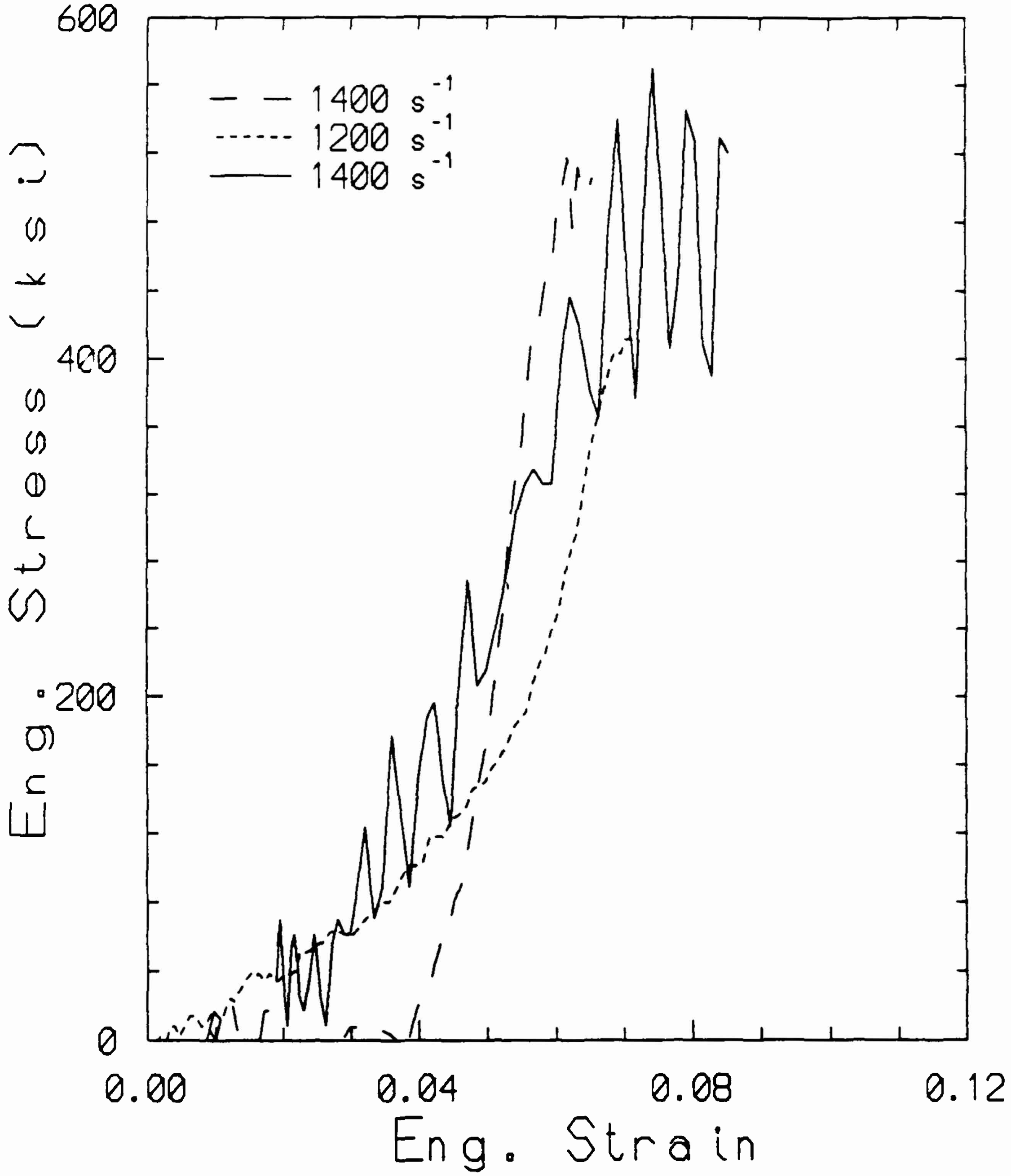

Figure 1.8. (a) Stress-strain curves for 10 inch drawback showing scatter in the data; specimen Type A (Tests 27, 33, and 36).

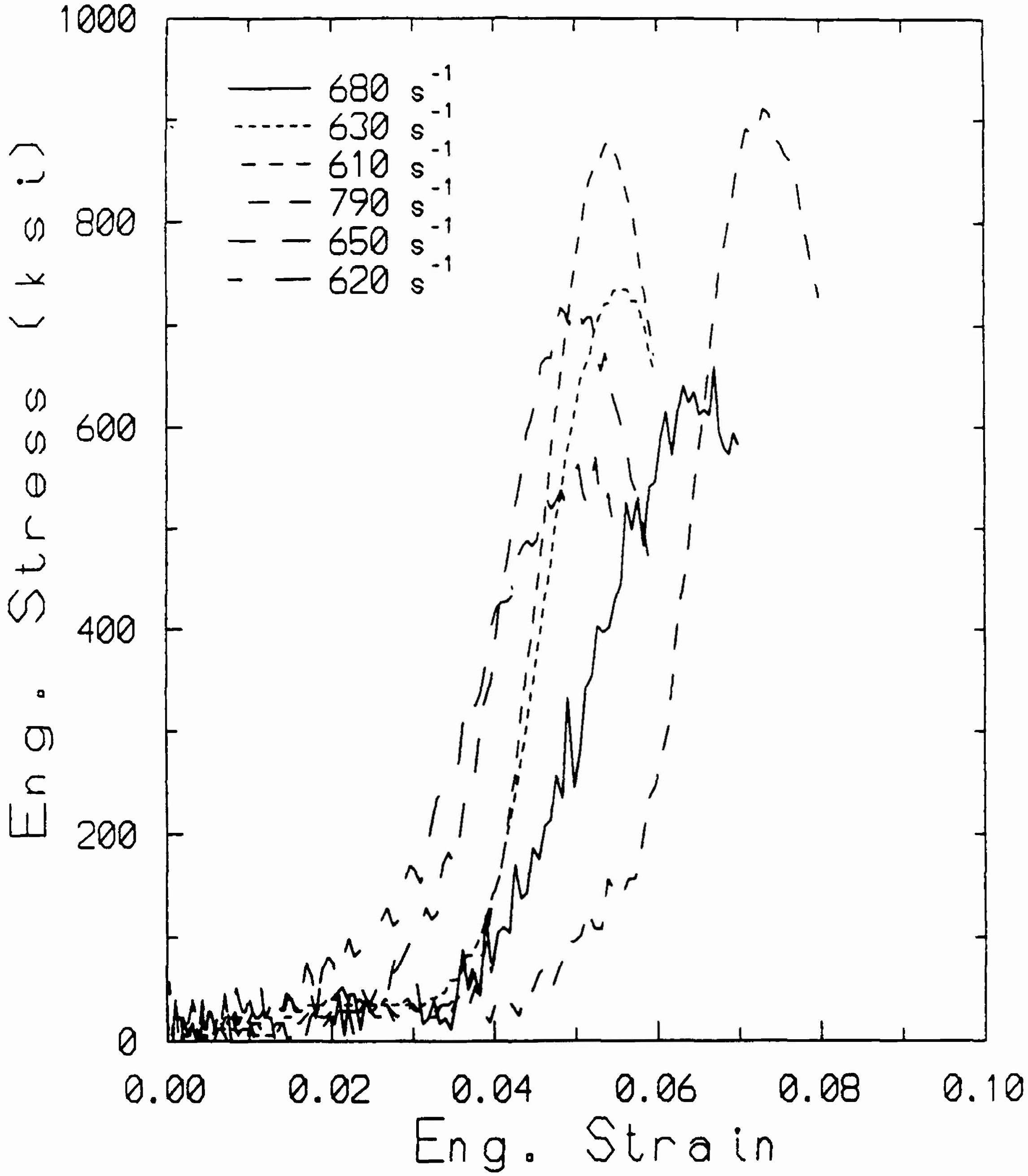

Figure 1.8. (b) Stress-strain curves for 10 inch drawback showing scatter in the data; specimen Type B (Tests 28, 30, 31, 32, 34, and 35).

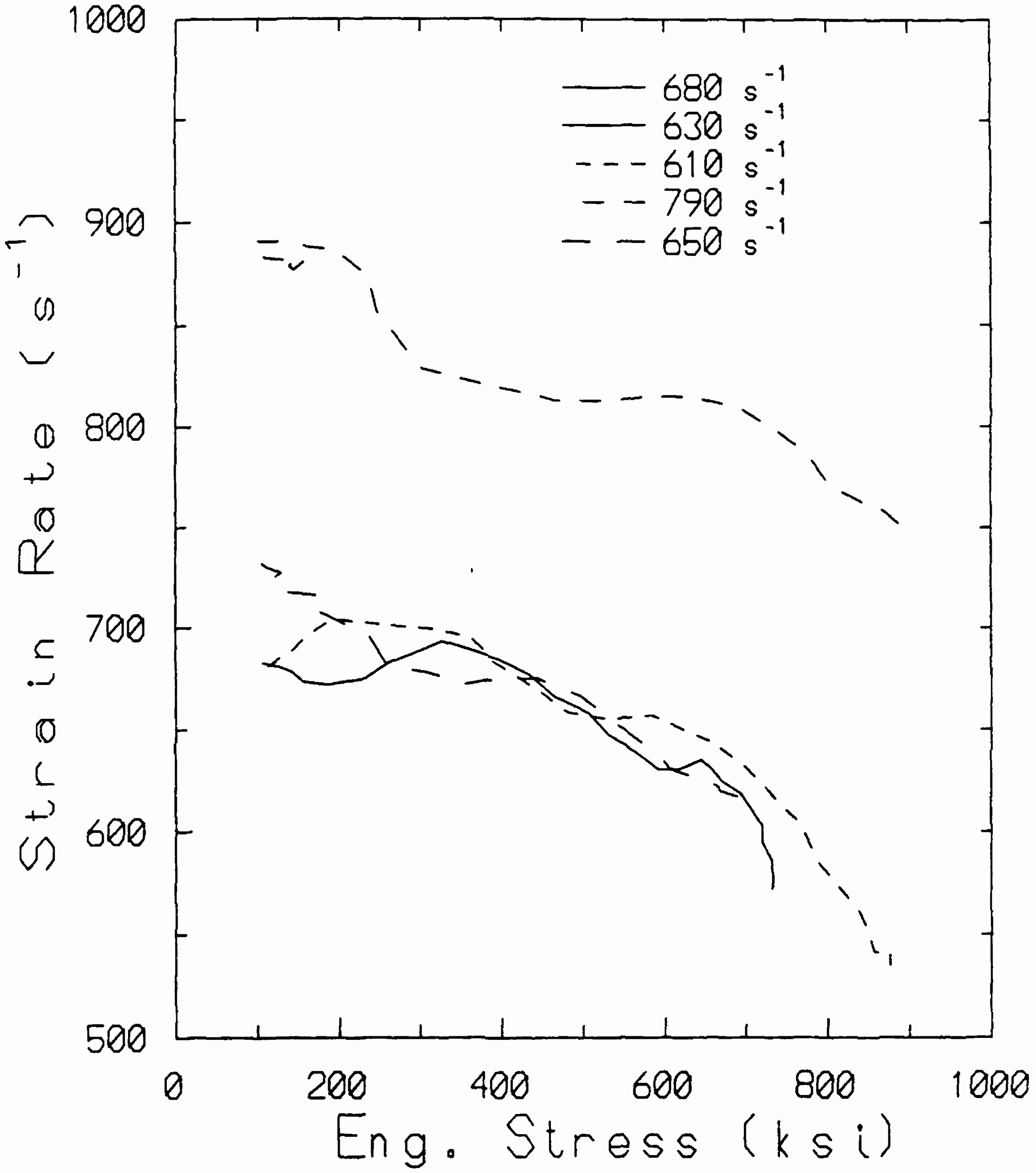

Figure 1.9. Stress-strain rate for 10 inch drawback and 60 bundles specimens, showing scatter in the data produced with Type B specimen (Tests 28, 30, 34, and 35).

SECTION 2

FORCE MEASUREMENTS ON PROJECTILES PENETRATING FIBER REINFORCED COMPOSITE TARGETS

A reverse impact technique that allows the force on projectiles penetrating fiber reinforced plastic (FRP) targets to be measured as function of penetration velocity was developed. Flyer disks of glass reinforced plastic (GRP) and Kevlar reinforced plastic (KRP) were integrated into a rather massive projectile package which was caused to impact stationary steel bars of flat, hemispherical, and conical nose shapes. The stress in the bar was measured by means of in-situ piezoresistive manganin gauges. For flat bars the force was steady. For hemispherical and conical bars the force was transient for thin flyers, showing an embedment stage and an exit stage. With sufficiently thicker flyer plates the force was steady, although for the hemispherical case the force was also oscillatory. This suggests markedly different penetration mechanisms, especially for the flat case. The energy dissipated in penetration was found to increase with impact velocities above the ballistic limit of the FRP.

1. INTRODUCTION

Fiber reinforced plastics (FRP) have many applications in light weight armor technology. The design process would be improved by a predictive model for penetration. A most advantageous approach to improved armor design is a predictive model which is based on material properties, since the properties of FRP composites can be extensively altered through process control.

A requisite to the development of accurate penetration models is the accurate measurements of forces on projectiles and projectile deceleration. Bless and Hartman[12] observed that the ballistic limit (V_{50}) of S-2 Glass® plates impacted by fragment simulating projectiles (FSP) of two diameters 7.62 mm (0.3 inch) and 12.7 mm (0.5 inch) is directly proportional to the plate thickness (T) to projectile diameter (D) ratio (T/D). This implied that the force on the projectile varied as the product TD, and was independent of impact velocity (above V_{50}). This was consistent with their hypothesis that failure by shear was a likely scenario for penetration; however, based on their measurements, the effective compressive strength of GRP was only 70 percent of the measured value. This discrepancy was resolved by suggesting that in fact there are two distinct penetration mechanisms: (a) cavity formation due to compressive punching and (b) delamination and tensile failure of fibers in the back of the target.

Zee et al.[13] measured the rigid body velocity history of conical projectiles (apex angle of 50 degrees and diameter of 6.35 mm (0.25 inch)) impacting woven fabrics of polyethylene (0.16-inch, 0.32-inch, and 0.48-inch thick). Their results indicated that the force on the projectile varied linearly as the penetration velocity, the peak force varied linearly with impact velocity, V_S, but was independent of target thickness.

Later Hsieh et al.[14], using the technique described in [13], measured the energy loss of conical projectiles (apex angle of 50 degrees) caused to impact 21.6 cm (8.5-inch) square plates of PE Spectra®-900, and Kevlar®-49 at velocities of 310 m/s (1017 ft/s) and 10 m/s (33 ft/s). They found (a) that for Spectra-900 the energy ($1/2m_pV_S^2$) was linearly proportional to target thickness, and that for high velocity impacts the energy gradient ($\partial E/\partial x$) was constant for a given thickness, suggesting that the force, F, on the penetrator was constant and was not a function of penetration velocity; however, for low velocity impacts the energy dissipated was not linear with thickness, (b) that for Kevlar the force appeared to increase with thickness, and (c) that for both Kevlar and Spectra the force appeared to decrease with impact velocity.

Woodward and Crouch[15] proposed a two-stage model for the perforation of laminated metallic composites by fragment simulating projectiles (FSP): stage I involves the formation and acceleration of plug and the concurrent deceleration of the projectile caused by reaction force. A one-dimensional wave propagation analysis was applied to this stage. Stage II involves the eventual shearing off of the plug and is realized when the projectile and the plug move with the same velocity. Their approach was to measure the composite strength in shear (blanking tests), in bending (four point bending test), in tension (tension test), and in compression (constrained compression test), as well as the interlaminar strength (four point bending test). Treating all these failure modes they predicted ballistic limits which are in marginal agreement with the measured data but which improved as the T/D ratio was increased. Probably for high T/D ratios stage I is the predominant stage of penetration, and this stage involves compressive forces which are measured relatively accurately.

Egglestone et al.[16], by performing quasi-static uniaxial constrained compression punching tests, were able to measure the energy required to perforate a target plate as a function of depth of penetration. The energy they derived from the measured force-displacement curve was much less than that at the ballistic limit, E_{50} $(=1/2m_pV_{50}^2)$, and no direct correlation between the two could be discerned.

In this chapter we propose a technique which is based on reverse impact which enables the measurement of the force acting on the projectile as it penetrates GRP and KRP targets at essentially constant velocity. These measurements are essential to any penetration model as they provide data for the variation of force as a function of velocity.

2. MATERIALS AND EXPERIMENTAL TECHNIQUE

A. Materials

The composites used in this study were S-2 Glass® phenolic supplied by Owens/Corning Fiberglas Co., Granville, OH, and Kevlar®29 Aramid reinforced plastics supplied by Dupont. GRP and KRP Flyer disks of about 44 mm (1.75 inches) in diameter and 12.7 mm (0.5 inch) in thickness were used in the reverse impact experiments in addition to 37.4-mm thick (70 plies) KRP flyers. The density and some mechanical properties of GRP and KRP are given in Table 2.1.

Table 2.1

Material Properties

	S-2 Glass®	Kevlar®29 Aramid
Density (kg/m^3)	2482	1441
Strength (MPa)	3724	3621
Modulus (GPa)	86	83
Toughness (MPa)	83	83

Bars of RC30 4340 and maraging steel of yield strengths of 862 MPa (125 ksi) and 2069 MPa (300 ksi), respectively were used as targets. There were three nose shapes: flat, hemisphere, and cone. The bars all had a diameter of 7.62 mm (0.3 inch). The bar wave velocity was ~5 mm/μs.

B. Experimental Technique

Figure 2.1 depicts a schematic of the reverse impact experiment. A rather massive projectile package incorporating a front FRP disk was caused to impact the stationary steel bar target (shown flat nose in Figure 2.1). The 50 mm gas/powder gun was used to launch the projectiles. The projectile mass was about 20 times the bar mass forcing the bar to indent itself in the FRP flyer at practically constant velocity, the impact velocity. The stress was measured by means of piezoresistive manganin gauges (Micro-measurements Type C-880113-B). A strain gauge was also mounted on the front bar to derive stress from strain measurements (in the elastic range) as an independent check on the directly measured stress from the manganin gauge.

3. RESULTS AND DISCUSSION

We performed ten reverse impact shots: six with GRP and four with KRP. Table 2.2 summarizes the impact velocity, the peak force results, the bar configuration from each shot, and the energy dissipated through penetration in each of the first eight shots.

Figure 2.2 shows the stress history from the gauge records with a flat, hemispherical, and conical end projectile, corresponding to shots 7-1618, 7-1619, and 7-1620, respectively, impacted by 12.7-mm thick GRP flyers. Records from the other three GRP shots were similar to those given in Figure 2.2.

Figure 2.2 shows that the peak force was the same irrespective of nose shapes. Figure 2.2 shows a steady force profile for the flat end bar (the same is true of shot 7-1624). The hemispherical and conical profiles were transient; in each case the profile showed an embedment and an exit stage. These profiles suggest markedly different penetration mechanisms, especially for the flat nose. In the case of a flat bar impacted by GRP flyer the mechanism of shearing appears to be dominant, whereas in the conical and spherical bars it is predominantly radial compression. The deviation from steady state penetration for the conical and hemispherical shots might be due to onset of flexure induced delamination, the depth of which varies with flyer stiffness, which varies as cube of the thickness. Indeed in shots 7-1649 and 7-1654 thicker (37.3 mm) KRP flyer plates were used.

Table 2.2

Summary of Results

Shot No	V_S (m/s)	Bar Shape	Bar Configuration (length in mm)	Flyer Mat'l Thick (mm)	Peak Stress (kbar)	Energy Loss (J)
7-1618	613	flat	76.2+g+76.2	GRP/12.7	14	1048
7-1619	659	hemisphere	76.2+g+76.2	GRP/12.7	12	631
7-1620	615	cone (90°)	76.2+g+76.2	GRP/12.7	13	738
7-1624	544	flat	76.2+g+76.2	GRP/12.7	13	896
7-1625	598	hemisphere	76.2+g+76.2	GRP/12.7	11	603
7-1626	495	cone (90°)	76.2+g+76.2	GRP/12.7	~6	411
7-1627	608	hemisphere	50.8+g+76.2	KRP/12.7	8	521
7-1629	692	cone (45°)	50.8+g+50.8	KRP/12.7	~6	334
7-1649	685	cone (60°)	50.8+g+76.2+g +50.8	KRP/37.4	~10	
7-1654	673	hemisphere	50.8+g+76.2+g +76.2	KRP/37.4	~11	

Figure 2.3 gives the gauge records for the 12.7-mm thick KRP flyers. It is noteworthy that the peak force for the cone was 20 percent less than the value for the hemisphere. Figures 2.4 and 2.5 show the stress profiles in these shots. It should be noted that: (a) the force was steady, (b) the peak force was almost the same, (c) the release in both profiles came from the free end of the rearmost bar, and (d) the hemispherical profile was oscillatory. This oscillation for the hemisphere case was not associated with GRP.

According to reference [12] the force, F, on a projectile penetrating a FRP target is given by the following expression

$$F = \frac{\pi}{2} Y_T D_T$$

where Y_T is the effective transverse compressive strength of composite (70 percent of the measured strength of 774 MPa for GRP), D is the bar diameter, 7.6 mm (0.3 inch), and T is the target thickness, 12.7 mm (0.5 inch). This leads to F = 118 kN. This is double the peak force we get in shots 7-1618, 7-1619, and 7-1620 on GRP.

Figure 2.6 shows the dissipated energy as a function of impact velocity, V_S. Plotted are data from reference [17]. The energy loss from the current measurements was estimated from the measured force-displacement curve, that of reference [17] from the expression for the impact kinetic energy minus the residual kinetic energy, or $1/2m_p (V_S^2 - V_R^2)$, where V_S and V_R are the measured impact and residual velocity, respectively. In reference [17] the ballistic limits of flat, hemispherical, and conical nose (apex angle of about 36 degrees) projectiles 7.62 mm (0.3 inch) in diameter and weighing 4.8 g (typical mass of 30 caliber FSP) were determined to be 633 ± 13 m/s, 374 ± 26 m/s, and 342 ± 15 m/s, respectively. These are shown in the plot with error bars. In shot 7-1618 the impact velocity was about 613 m/s. As shown in Figure 2.6, the energy dissipated in this shot is in good agreement with that of reference [17] at the ballistic limit, suggesting a correlation between the current experiments and those of reference [17]. In Figure 2.6 the energy loss displays, at least for GRP, an increase with increasing impact velocities above V_{50}. This result agrees with the findings of reference [18].

4. CONCLUSIONS

Force measurements on projectiles of one diameter penetrating FRP reveal (a) that these measurements are compatible with the ballistic data of reference [17], (b) that the force varies as function of FRP thickness, suggesting that penetration mechanisms are effected by the target thickness, and (c) that the energy expended in penetrating a target increased with impact velocities above the ballistic limit.

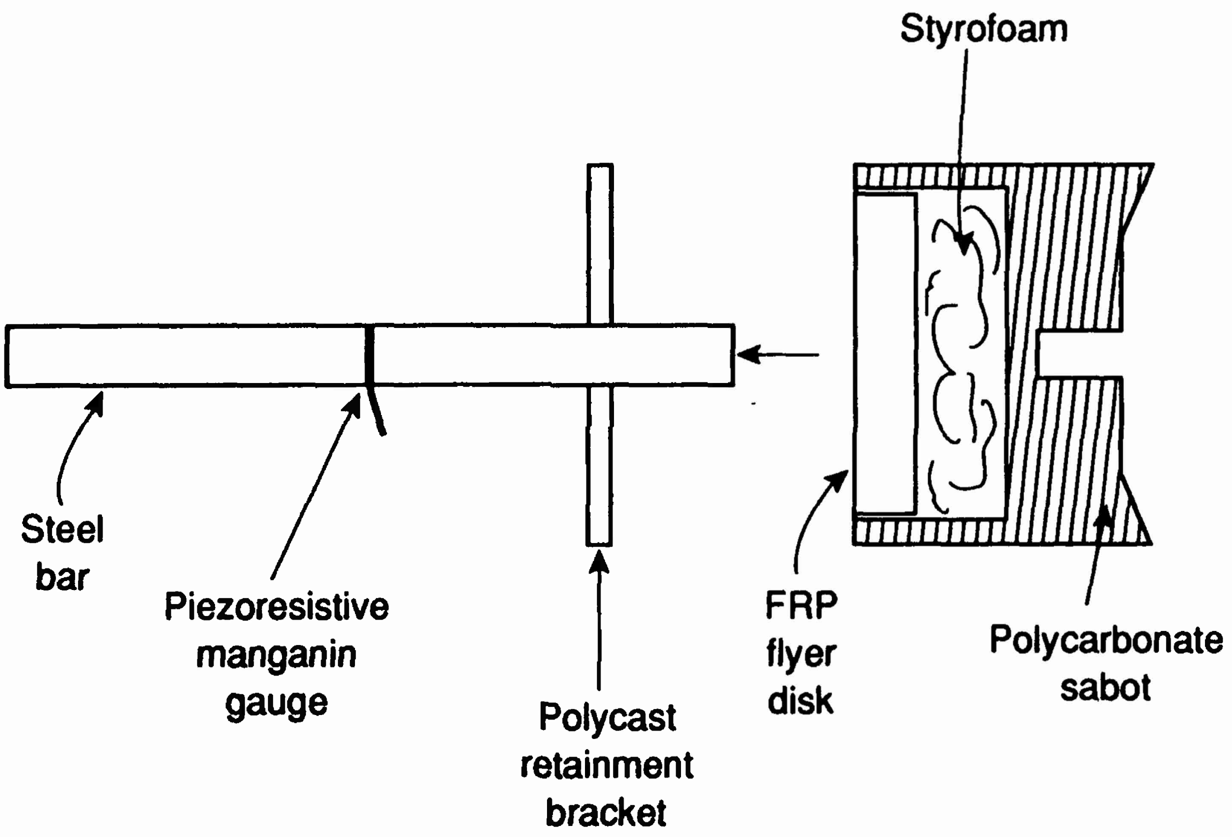

Figure 2.1. Schematic depicting FRP flyer and bar target in the reverse impact experiment.

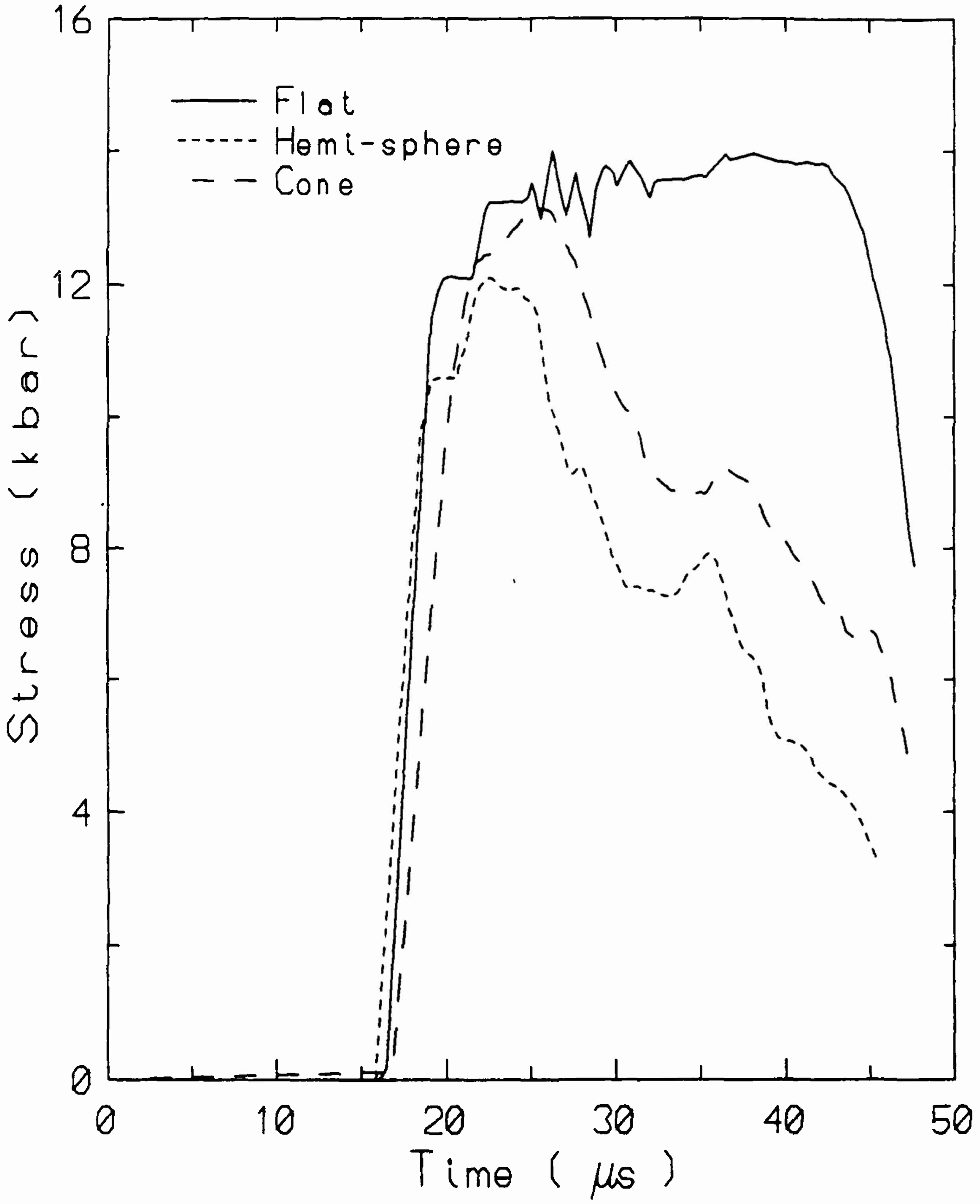

Figure 2.2. Manganin gauge stress history records for 12.7 mm thick GRP flyers impacting bars with three nose shapes: flat (Shot 7-1618), hemispherical (Shot 7-1619), and conical (Shot 7-1620).

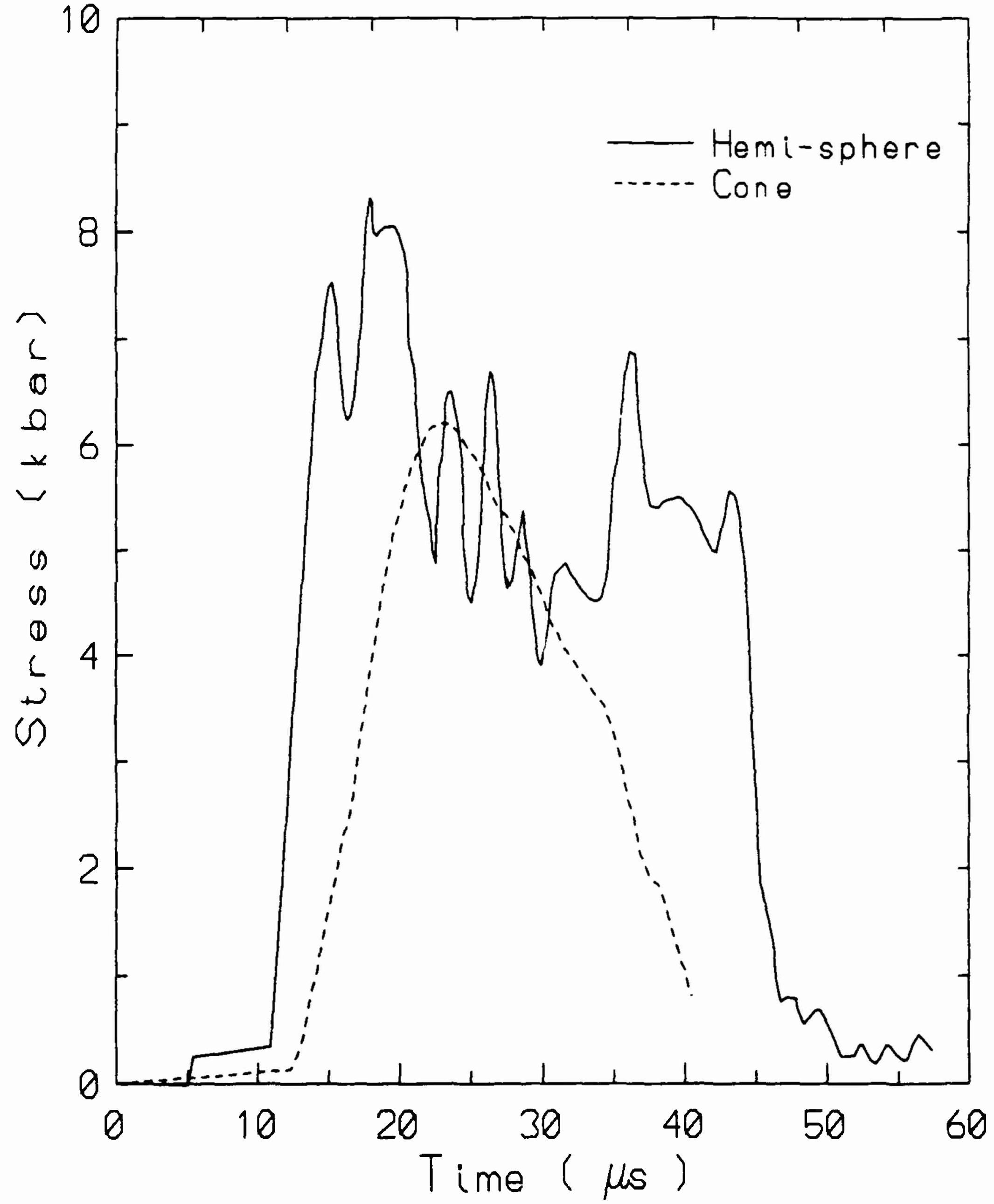

Figure 2.3. Manganin gauge stress history records for 12.7 mm thick KRP flyer and two nose shapes: hemispherical (Shot 7-1627) and conical (Shot 7-1629).

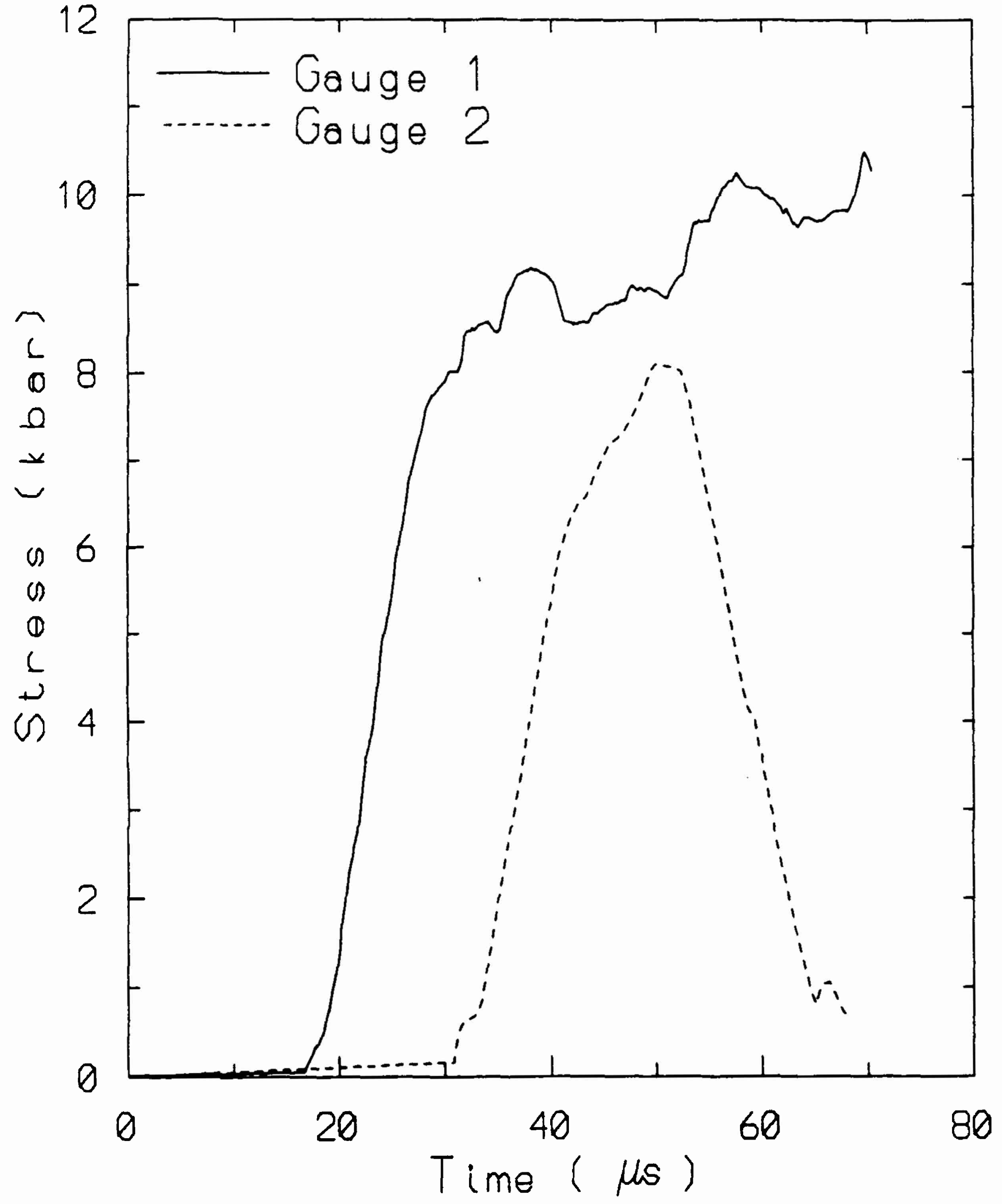

Figure 2.4. Manganin gauge stress history records for Shot 7-1649, showing steady state penetration into 37 mm thick KRP by a conical nose shape bar.

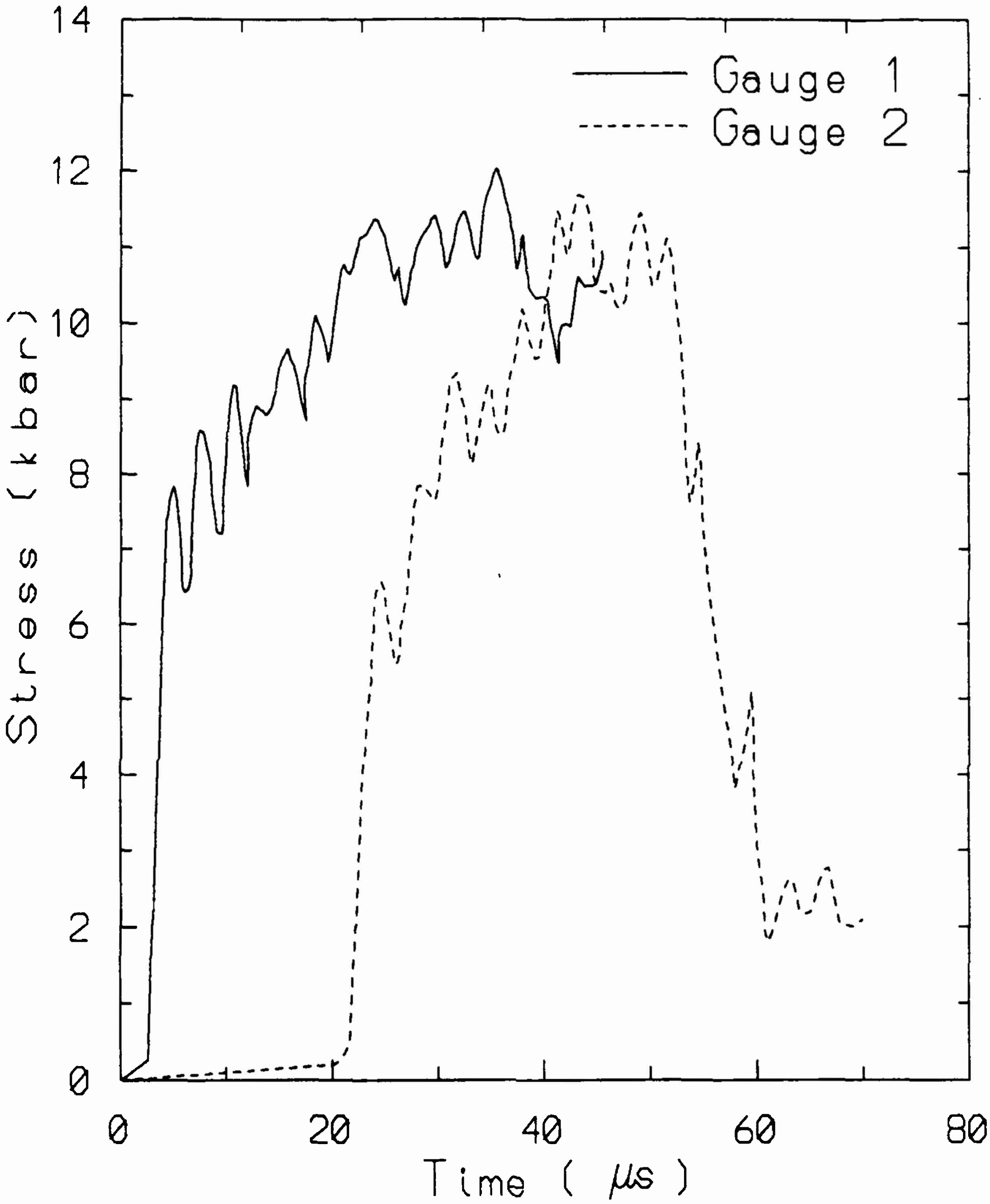

Figure 2.5. Manganin gauge stress history records for Shot 7-1654, showing steady state penetration into 37 mm thick KRP by a hemispherical nose shape bar. The force is oscillatory.

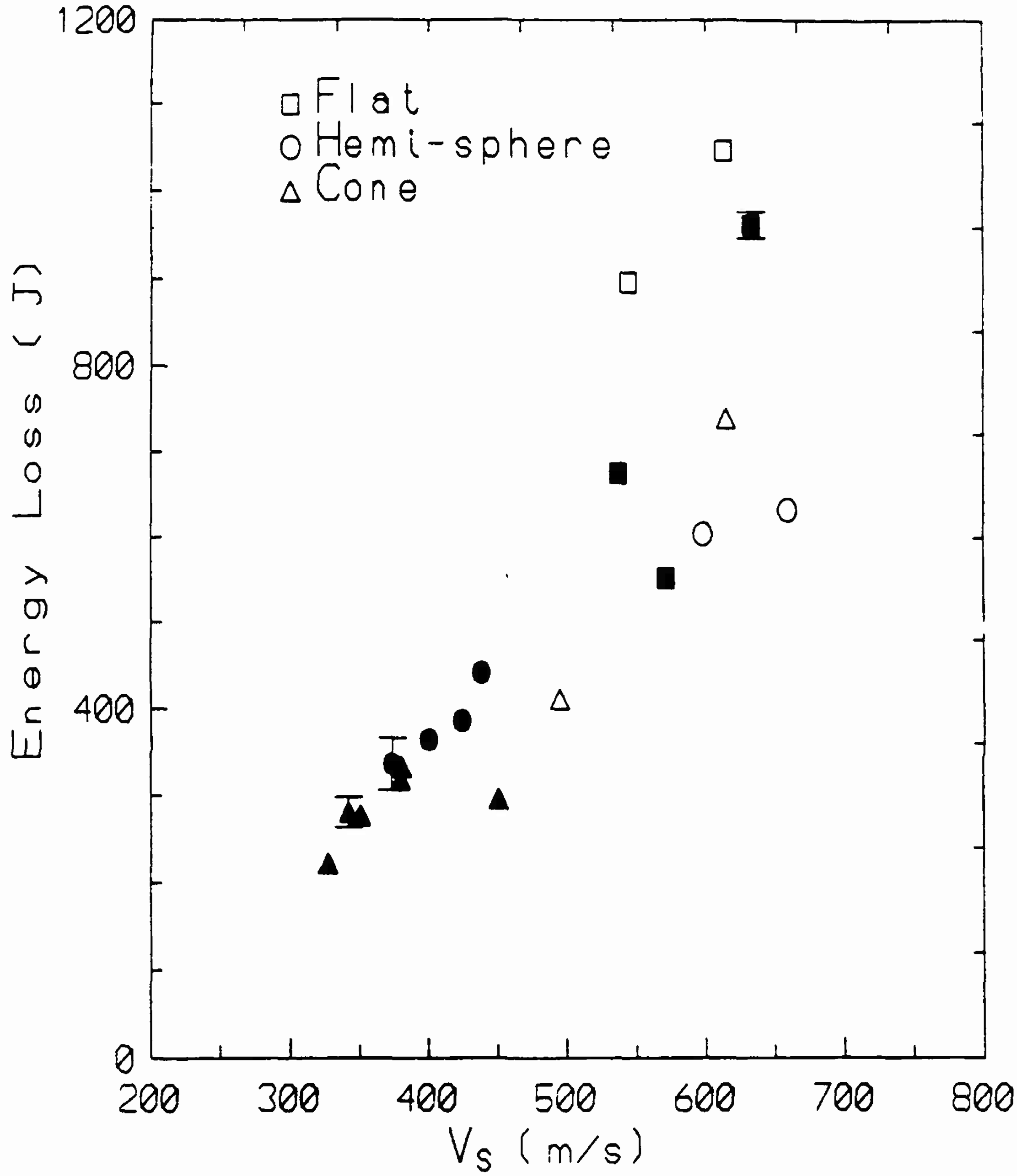

Figure 2.6. Energy loss as function of impact velocity from current data on GRP (open symbols) and from Reference 17 (solid symbols) on 12.7 mm GRP plates impacted by 7.6 mm diameter projectiles.

SECTION 3

BALLISTIC PENETRATION STUDY OF S-2 GLASS/PHENOLIC SPALL LINER MATERIALS

Ballistic failure of S-2 Glass® composites was studied by shooting projectiles with various nose shapes through 0.5 inch panels, by examining thick sections penetrated by shaped charge jets, and by conducting high strain rate testing on fibers with a split Hopkinson bar. There appears to be five penetration modes of failure of glass composites--shock, double shear, single shear, cavity expansion, and tensile stretching. Shock is a very important stage for blunt fragment simulators--amounting to about 30 percent drop in velocity. Double shear leading to cratering occurs near the surface for blunt projectiles. Cavity expansion occurs with sharp projectiles; the composite is relatively less effective for this mode. Shaped charge jets penetrate with the additional mechanisms of resin pulverization. Tensile stretching (membrane failure) dominates for blunt projectiles striking relatively thin targets. Hopkinson bar measurements of strength reveal a slight increase in bundle strength with strain rates characteristic of ballistic impact.

1. INTRODUCTION

Glass reinforced plastics (GRP) have found many applications in armor technology[19]. In spite of some past measurements of time resolved penetration[20], the connections between the mechanical properties of the composites and the penetration resistance remain obscure. Unlike metals, the properties of GRP composites can be greatly varied through controlled changes in process or composites. Thus, there is a large potential payoff for understanding the penetration process in GRP-like materials.

In this report we point out the different penetration modes of an armor-grade GRP-S-2 Glass® phenolic composite. We also report initial measurements of the dynamic strength of these fibers. From these observations, the importance of the various penetration modes may be quantitatively assessed.

2. EXPERIMENTS WITH FRAGMENT SIMULATORS

Modified fragment simulators were employed to study penetration of 12.7-mm thick (25-ply) GRP. Targets were fabricated by Owens Corning Fiberglas (OCF) by a licensed process designated HJ1. This complies with MIL-L-64154.

Targets were 150 mm square. The projectiles are sketched in Figure 3.1, which includes dimensions and masses. The material was Rockwell C-30 steel and deformation was minimal. They had various nose shapes. They were fitted with "tails" so that high-speed photography could be used to measure velocity while the projectiles embedded in the targets. Dynamic data included both the rear of the projectile (from which the nose position could be calculated) and rear surface of the target. In cases of complete penetration, residual velocities were also measured by flash x-rays.

Table 3.1 lists the data; SI units are used. The ballistic limits (V_L) of these projectiles varies considerably. For the flat projectiles, $V_L = 633 \pm 13$ m/s. For the hemisphere, $V_L = 374 \pm 26$ m/s. The conical projectile results display a zone of mixed results. The best value for V_L is 342 ± 15 m/s. Thus, the energy required to penetrate with the sharp projectile is only about 30 percent of the energy required to penetrate with the blunt projectile.

Figure 3.2 illustrates photographed cross sections of penetration cavities from shots that resulted in complete penetration. Refer to references [21] and [22] for additional examples of cavities.

Penetration of the projectiles was studies from streak and framing camera records of the tail motion. Figure 3.3 illustrates our findings for projectiles just above the ballistic limit. These data were reduced by manually identifying nodes in streak camera records of position versus time and assuming constant acceleration between nodes. The figures plot energy versus Lagrangian position. Lagrangian position is the position relative to the moving target. It is computed as

$$h = T - x_p + x_r$$

where x_r is the observed position of the rear of the target, x_p is the inferred position of the nose of the projectile, and T is the original target thickness (12.7 mm). It can be seen that the blunt projectiles undergo a large sudden deceleration on impact. This phenomenon was noted previously[20] and has been quantitatively attributed to the impact-induced shock

TABLE 3.1

Summary of Impact and Residual Velocities

Shot No.	V_S (m/s)	V_R (m/s)	Nose Shape
2202	243	0	cone
2204	283	0	cone
2216	314	0	cone
2217	326	0	cone
2203	327	120	cone
2218	351	89	cone
2220	357	0	cone
2219	381	79	cone
2221	373	NM	cone
2201	380	110	cone
2200	451	283	cone
2197	484	NM	cone
2199	545	NM	cone
2207	444	0	hemisphere
2223	400	91	hemisphere
2208	438	88	hemisphere
2206	424	138	hemisphere
2222	444	NM	hemisphere
2189	473	NM	hemisphere
2190	478	NM	hemisphere
2196.5	498	NM	hemisphere
2196	522	NM	hemisphere
2209	466	0	blunt
2210	520	0	blunt
2211	537	86	blunt
2213	571	310	blunt
2196	602	NM	blunt
2195	612	NM	blunt

wave. Beyond this event, the decrease of energy with penetration is approximately linear for all projectiles.

Based on observations of penetration cavities and projectile kinetics, we have identified five modes of penetration in GRP targets. The modes are sketched in Figure 3.4.

The first phase is shock loading. The peak pressure is determined by the relative impedances of the projectile and the target and the duration is approximately equal to the transit time of a shock across the flat face of the projectile.

The next stage is double shearing. Here fibers are cut twice and expelled out the front face of the target. Uncut portions of fibers are often bent outward. The upper region of the target around the cavity is delaminated and the surface is deflected outward.

The next stage is single shearing. Fibers are mainly cut once and the loose ends are left in the wake of the projectile. Near the surface, fiber ends are bent outward. Deeper in the target they are bent inward.

Cavity expansion refers to radial movement of the target away from the path of the projectile. This is the chief means by which metal targets are penetrated by sharp projectiles[23]. It is recognized in GRP targets by the occurrence of fiber kinking. In partially penetrated targets, kinking is much more severe so it appears that some spring back must occur after projectile passage or else kinking is suppressed at higher velocities.

At the exit face, fibers are always stretched. Failure appears to be in tension. There is often extensive delamination accompanying fiber stretching[22].

The extent of each penetration mode is different for the various projectile types. Examination of the partial penetration cavities in Figure 3.2 (a), (b), and (c) shows that the sharp projectile penetrates almost entirely by cavity expansion. The hemispherical nose projectile penetrates mainly by double cutting followed by cavity expansion followed by stretching. The blunt projectile penetrates by shock, followed by double cutting, followed by single cutting, followed by stretching.

We have conducted ballistic experiments on many other types of fibers. Qualitatively, the penetration modes described above are observed in all composites when the thickness of the target exceeds the diameter of the projectile. We have not yet made quantitative examinations of cavities in other fiber reinforced composites.

3. OBSERVATIONS OF SHAPED CHARGE JET CAVITY

GRP has also been found to be an effective armor against certain shaped charged jets[24]. We have examined shaped charge jet cavities in very thick GRP to see if the penetration mechanisms were also described by Figure 3.4. Figure 3.5 illustrates a cross section through the cavity.

There is a clear cavity whose mean diameter is about 5 mm. Unlike the lower velocity penetration cavities, the resin around the cavity out to about 5 mm has apparently been pulverized and removed. There is some kinking, or at least tufting, of fibers just beyond the pulverization region. Note that shock velocities in these materials are about

3 mm/μs, so the jet penetration is almost certainly supersonic; hence, there would be a bow shock. Therefore, we hypothesize that the target out to a diameter of about 15 mm from the center line has been severely degraded by shock. Fibers around the cavity out to about 10 mm are unsupported. Fibers are bent along the path of the penetration, making an angle of 10 or 20 degrees to the ply layup. Very few fibers sections were found in the cavity, but the ones present were 3 to 5 mm long. This leads us to conclude that the fibers are double cut. There is almost no evidence of delamination. There was no trace of copper or molten glass in the cavity.

Overall, the penetration mechanism for a shaped charged jet does not resemble that of a low speed projectile. The most essential difference is the pulverization of the resin. Double cutting of the unsupported fibers is probably due to their inability to move out of the way of the jet because of inertia, rather than the jet tip geometry (as with steel projectiles).

4. HIGH STRAIN RATE TESTS

A split Hopkinson bar was used to measure the dynamic tensile strength of fibers to determine if failure of glass bundles is rate dependent. S-2 Glass® roving with 463 sizing was supplied by OCF. A tow of this roving consisted of 20 strands; there were 204 filaments per strand. Specimens were prepared from single strands that were extracted from the tow. OCF has measured the static tensile strength of S-2 Glass® 463 roving (average of 30 tests) as 36 kbar (535 ksi) with a variance of 3 percent and that of monofilament (average of 128 tests) as 49 kbar (713 ksi) with a variance of about 1 percent. The spall strength of soda lime glass, which may represent the upper practical limit for strength of structureless glasses, is about 60 kbar[25].

Two fixture designs were employed in order to gain confidence in the results. Type I was a split spool design while Type II was a straight pull. The fibers were encased in epoxy resin except in the gauge sections. High-speed photographs and post test analysis of successful tests confirmed that almost all fibers broke in the gauge sections.

Figure 3.6 shows a typical stress-strain result for Type II. The strain to failure is about 5 percent, which is very close to the static value. However, we believe that the strain is overestimated in these calculations because we assume that all strain takes place within the gauge length, whereas in fact some strain probably occurs in the epoxy tabs adjacent to the gauge length. The decay from maximum stress also takes place over a range of strain. We attribute this width of the peak to the distribution of strength and/or slack among the several thousand filaments that make up the two tows that were tested. Over the range of strain rates tested (650 to 1000/s) there was no discernable variation of strength with strain rate.

Over the range of strain rates tested (600 to 1000/s), no systematic variations with strain rate were detected. In Figure 3.7 strength is plotted versus number of bundles in the test. We have also included tests with Type I specimens in which not all gauge sections ruptured; for those, we corrected the sample cross section for this effect. In two tests there were two load peaks; in those experiments we assumed that there were two families of fibers with different slack but same strength and corrected the computed peak stress accordingly.

The spread of strengths runs from 62 to 31 kbar. The average strength based on all tests was 42 kbar (606 ksi) with a standard deviation of 25 percent. The Type I (spool) specimen usually gave lower results. If we only use Type II specimen data, then the mean is about 48 kbar (700 ksi). This is slightly higher than the static value. We suspect that the higher strengths in some of our tests are more characteristic of rapidly failed bundles and the lower values are affected by the overlaying of bundles in the fixtures.

We intend to continue this test using impregnated filaments and other types of fibers.

5. ANALYSIS

The drop in velocity, ΔV, in the shock phase can be explained by the following model. The peak shock stress is given by

$$\sigma_m = \frac{Z_p Z_t V_s}{Z_p + Z_t}$$

and the drop in momentum of the projectile is given by

$$g D_p^3 \rho_p \Delta V = \frac{1}{4} \pi D_p^2 \sigma_m t_d$$

where V_s is the impact velocity, Z_t and Z_p are the shock impedances of the target and projectile, and g is the shape factor of the projectile, defined so that the mass of the projectile $M_p = g D_p^3 \rho_p$ (D_p and ρ_p are projectile diameter and density) and t_d is the shock duration.

If we take the shock duration t_d to be twice the transit time through the projectile, it follows that

$$\frac{\Delta V}{V_s} = \frac{\pi Z_t (\frac{L}{D})_p}{2g(Z_t + Z_p)}$$

where $(L/D)_p$ is the aspect ratio of the projectile. Z_t = 80 kbar/(mm/μs) (measured), Z_p = 470 kbar/(mm/μs), and g = 1.4 for the blunt projectile, giving $\Delta V/V = 0.27$.

Since $\Delta V/V = 1 - (E_2/E_1)^{1/2}$ (where E_2/E_1 is the ratio of post- and pre-impact projectile energy), one derives from Figure 3.3 that $\Delta V/V = 0.25$, which is very close to the model value.

Values of $\Delta V/V$ are much less for the hemispherical nose and conical nose projectile. This is because the duration of the shock in this projectile is much less due to the smaller diameter over which the projectile is effectively flat.

Forrestal and Rosenberg[26] developed an approximate but accurate perforation model based on Hill's formula for the stress required to expand a cavity in a ductile metal[27] using a von-Mises yield criterion:

$$\sigma_c = \frac{Y}{\sqrt{3}}[1 + \ln(\frac{\sqrt{3}}{5 - 4\nu} \cdot \frac{E}{Y})]$$

From this, it follows that

$$V_L = \sqrt{\frac{2\pi r^2 T \sigma_c}{M_p}} = \sqrt{\frac{2T\sigma_c}{\rho_p(L + h/3)}}$$

where the last term is specific for a conical projectile of shank L and nose length h.

This equation might be expected to apply to our conical projectiles. We note, however, that it cannot apply to the fsp projectiles, since V_L for these projectiles is proportional to T/D[20,21]. In the equation above the limit velocity is proportional to $(T/D)^{1/2}$.

The prediction of ballistic limit was rather close, V_L = 398 m/s versus the measured value of 342 m/s.

There are high strain rate data for compression[28] and tension[29] that show slight increases in properties of GRP with strain rate. However, in order to bring the predicted and measured values of ballistic limit and residual velocities into agreement, it is necessary to assume a strength of 24 ksi. Thus, the performance of GRP against sharp projectiles is less than would be predicted from metal-like behavior. In order to resolve this discrepancy, it will probably be necessary to assume either a strain-softening behavior of the GRP or take into account the initial slack, over which strain takes place at very low stress.

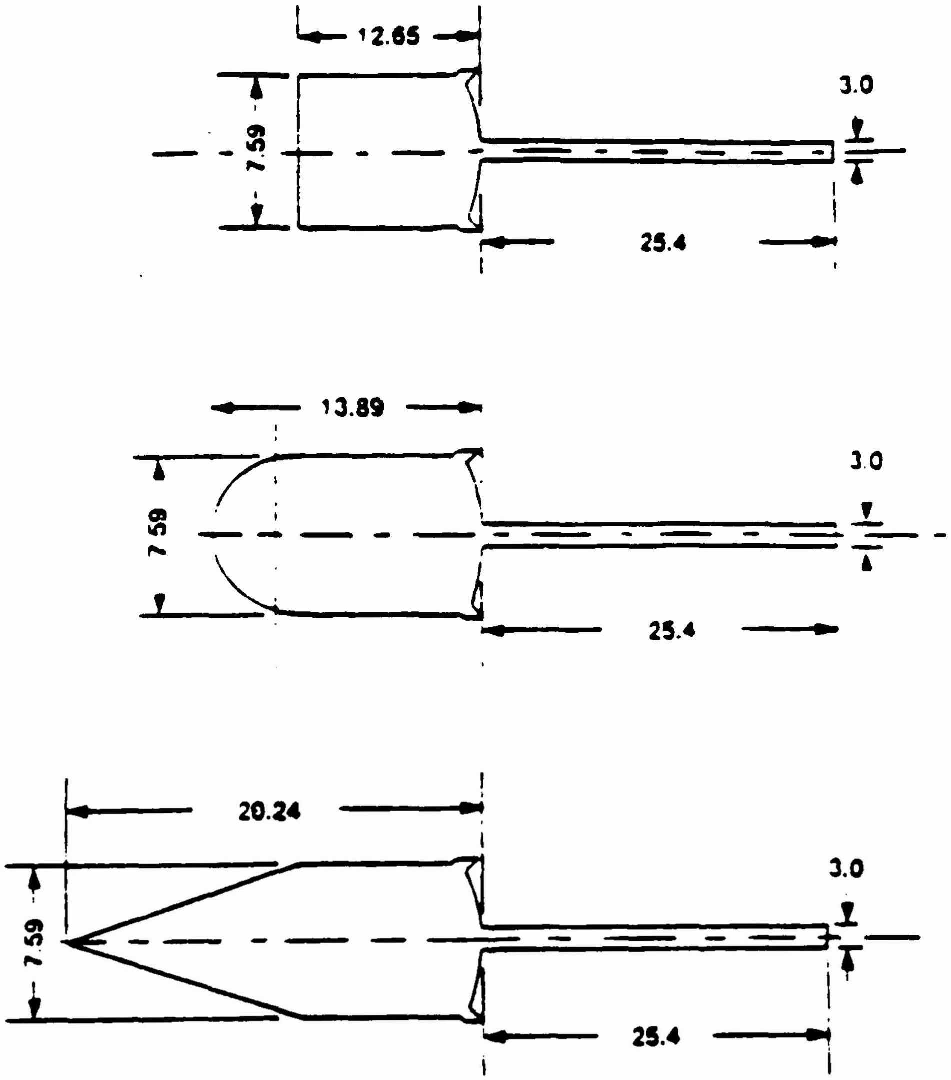

Figure 3.1. Sketch of projectiles used in this study. Bodies and tails were HR30 steel. Projectile masses were 4.81 ± 0.1 g.

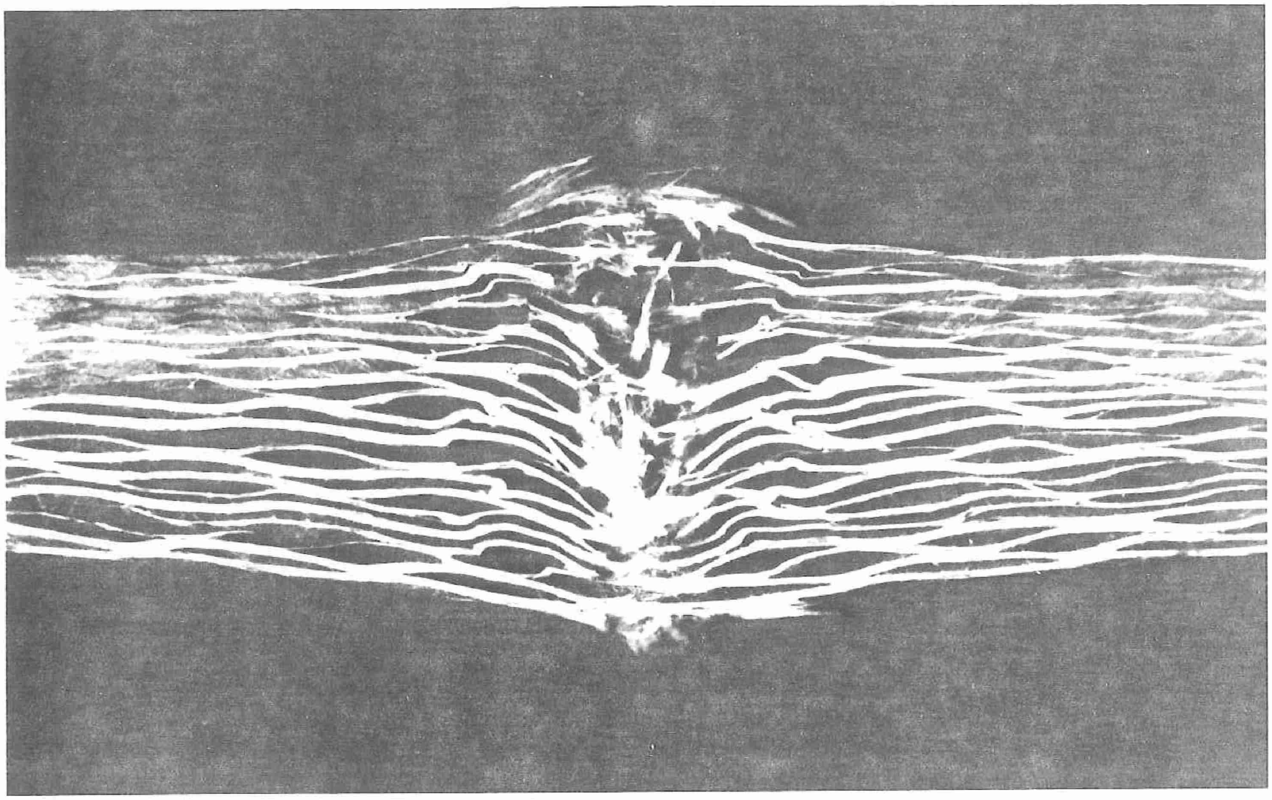

Figure 3.2. (a) Cross-section of lowest complete penetration shot with a cone nose.

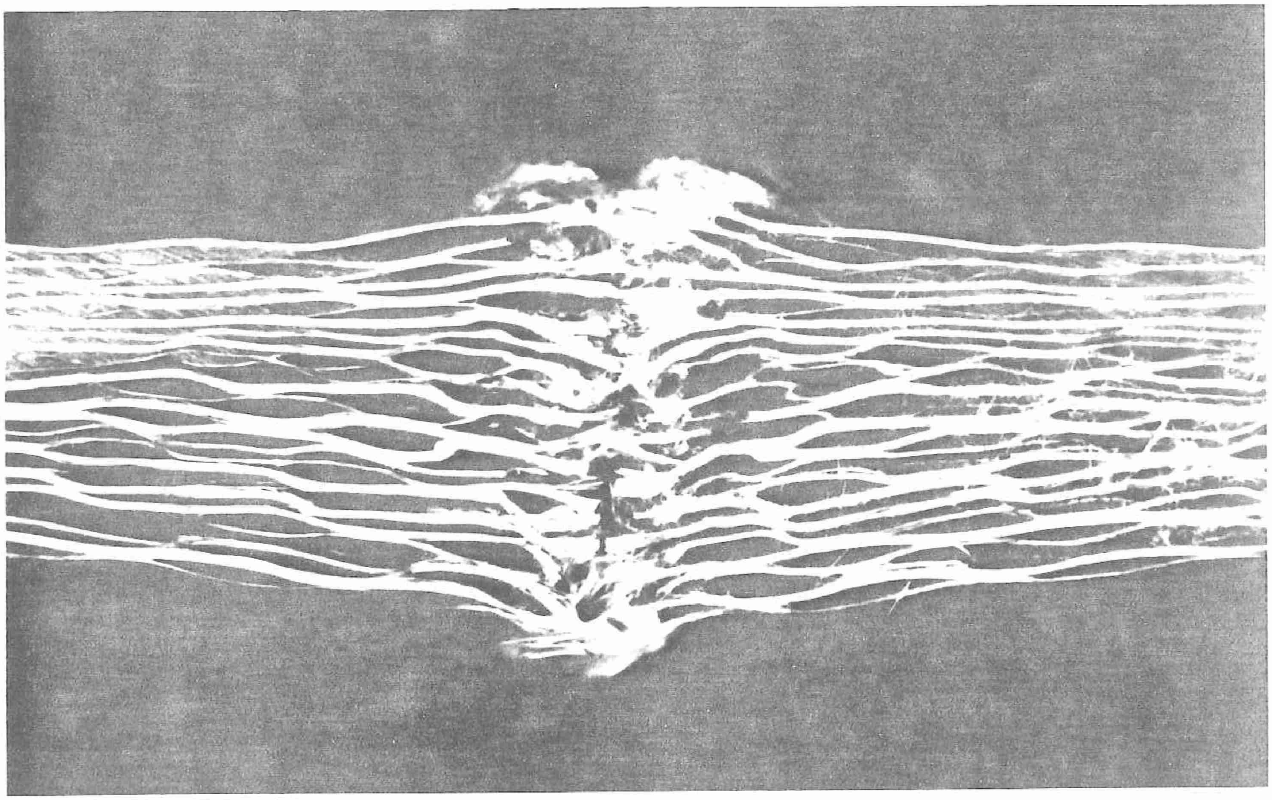

Figure 3.2. (b) Cross-section of lowest complete penetration shot with a hemispherical nose.

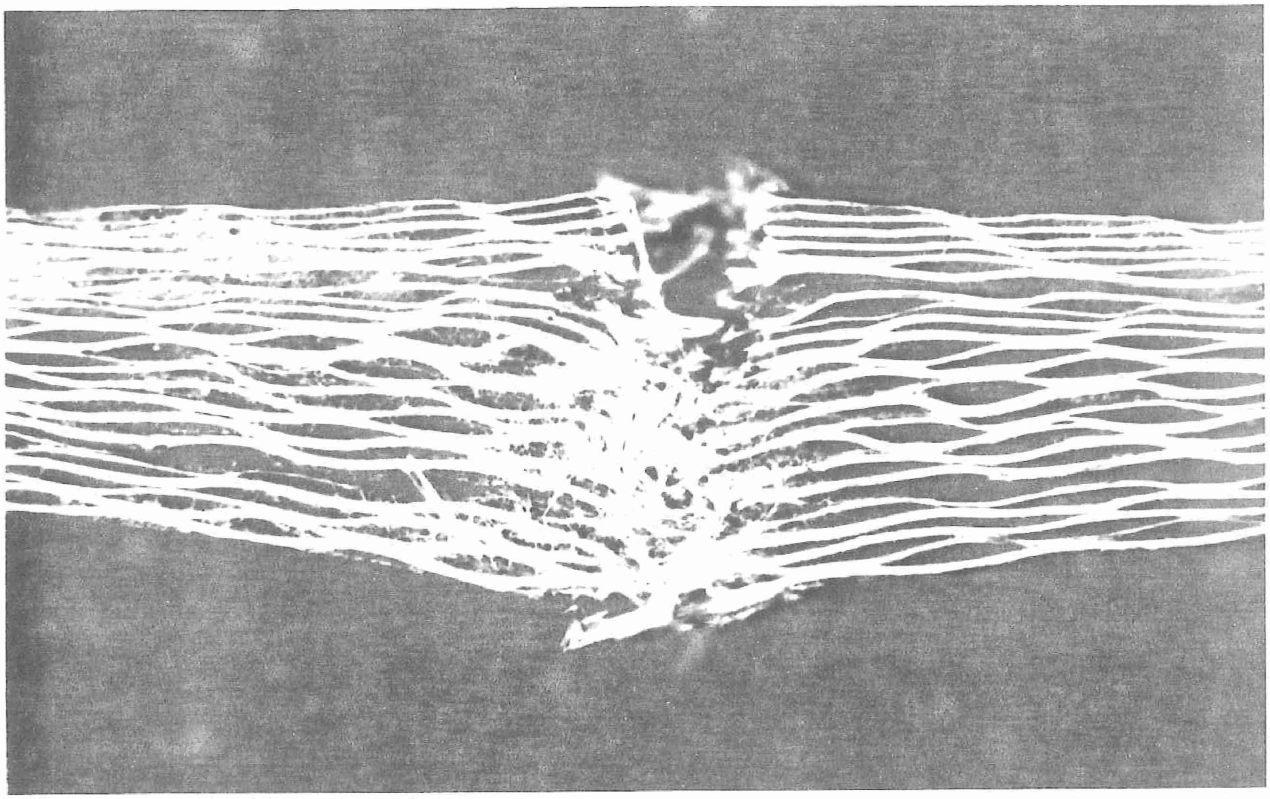

Figure 3.2. (c) Cross-section of lowest complete penetration shot with a blunt nose.

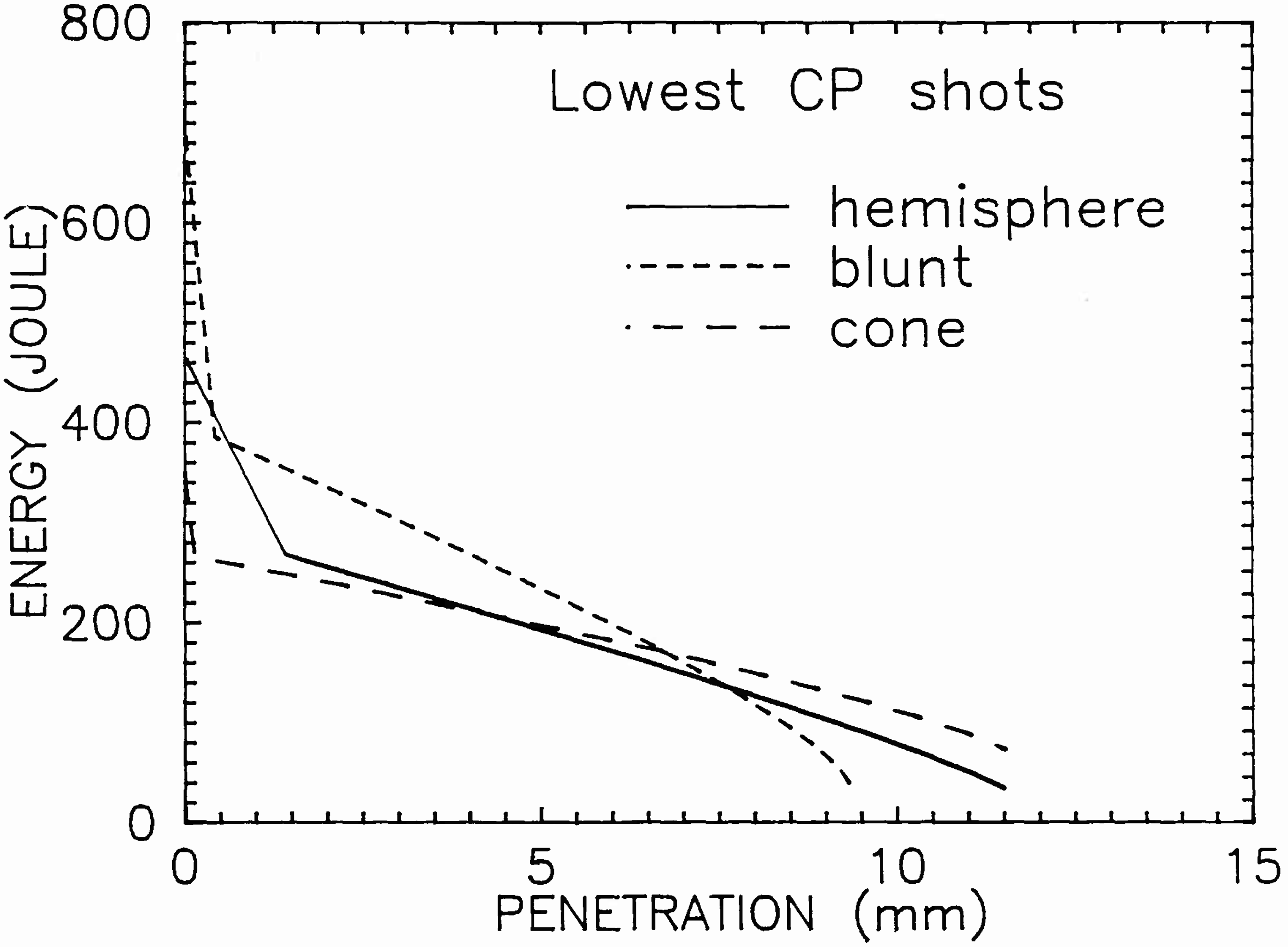

Figure 3.3. Energy versus penetration for lowest complete penetration shots.

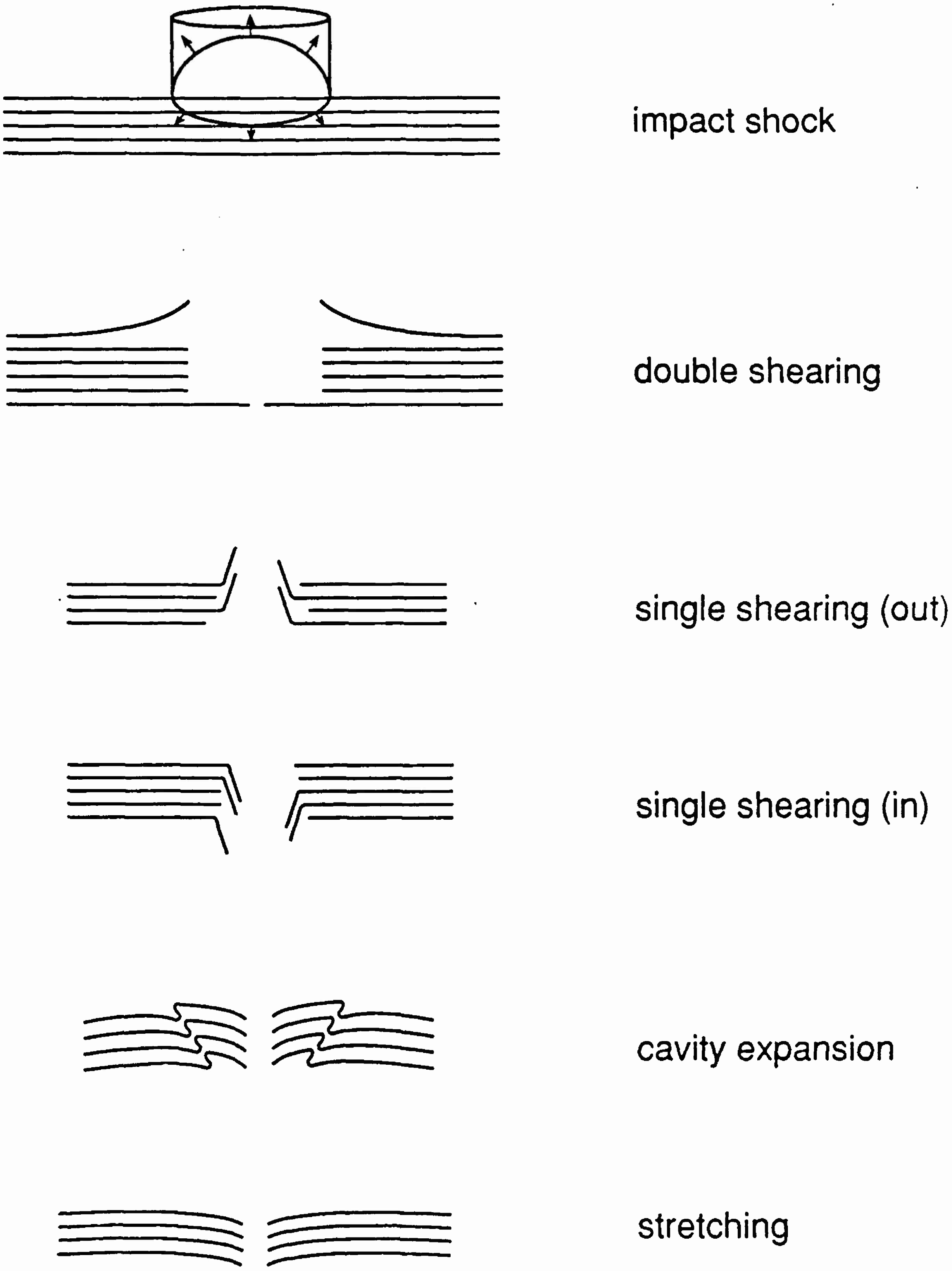

Figure 3.4. Penetration modes in GRP targets.

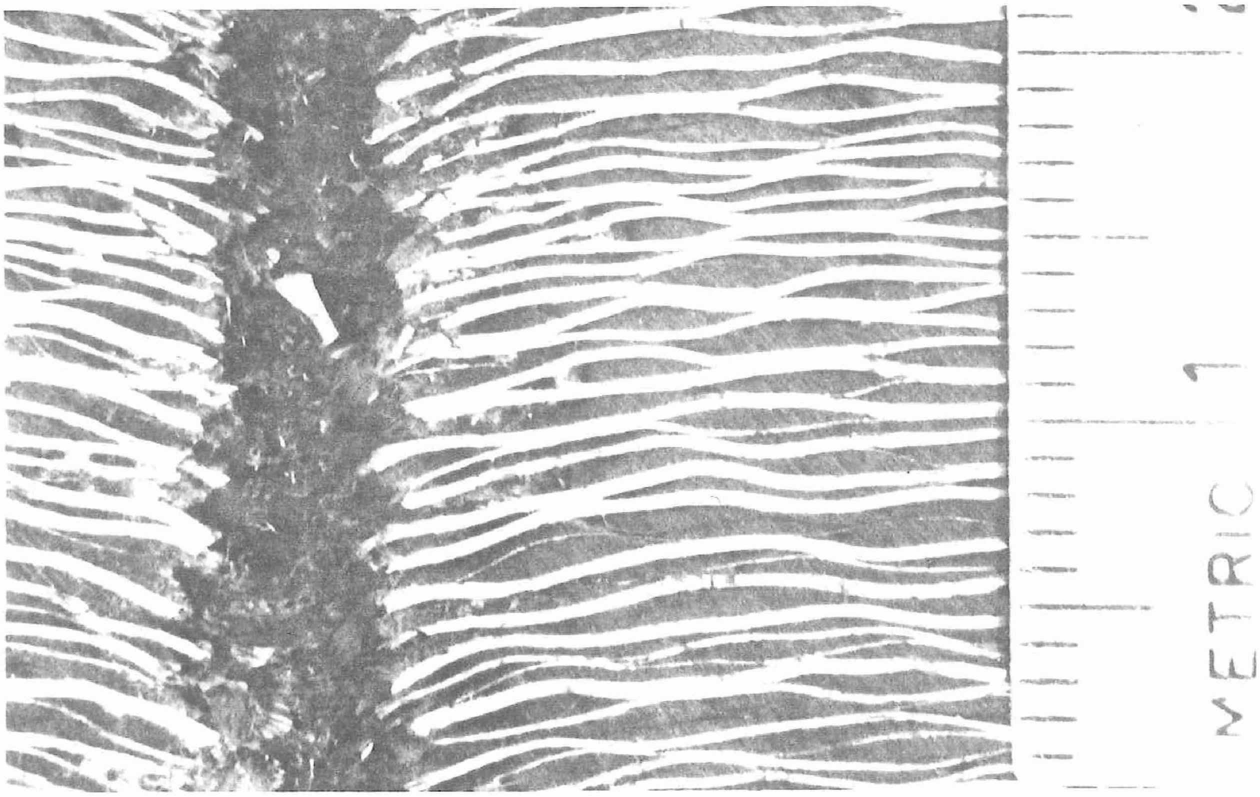

Figure 3.5. Cross-section in cavity of target penetrated by a shaped charge jet.

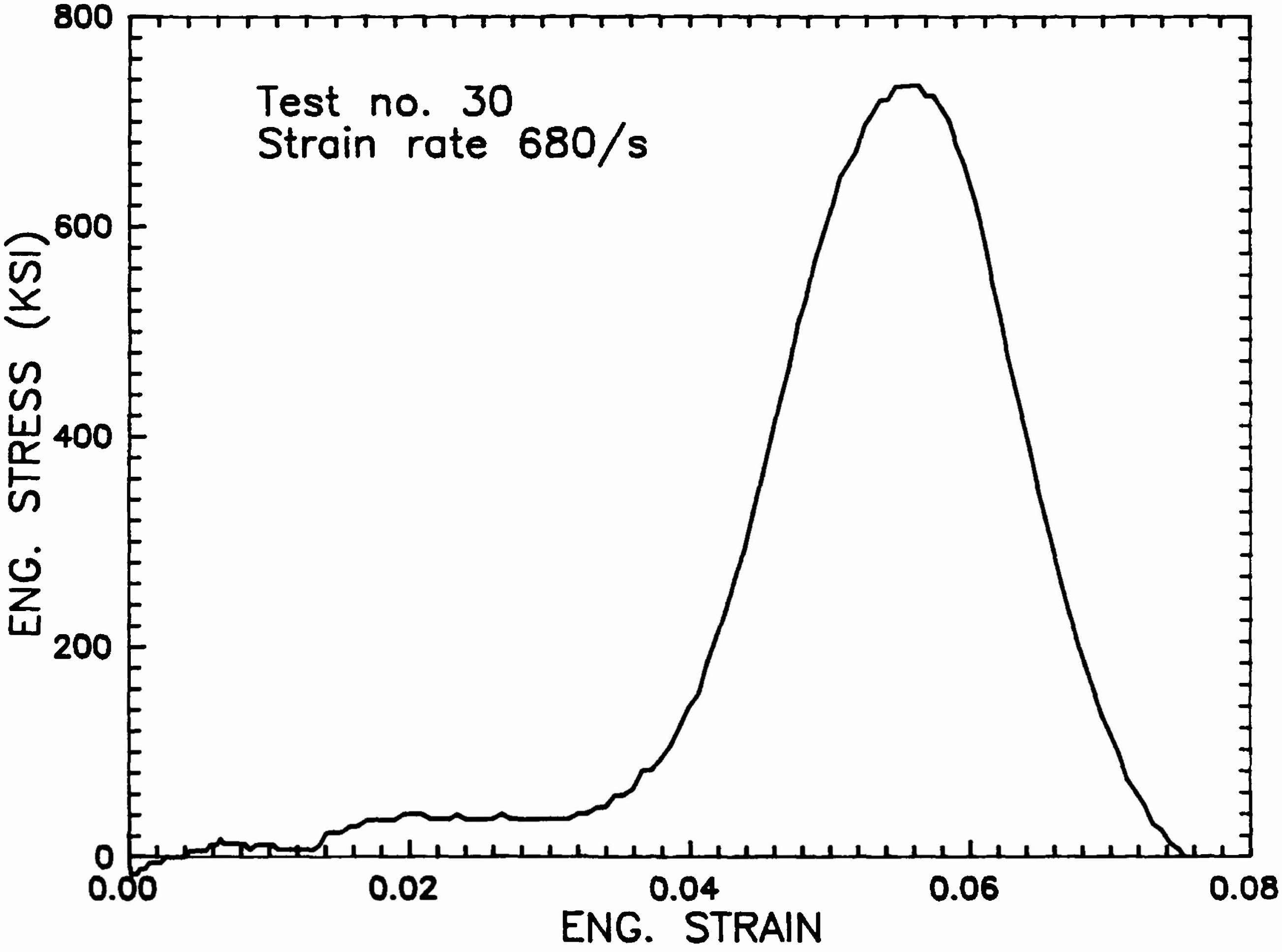

Figure 3.6. Typical stress-strain curve for Type II test with split Hopkinson bar.

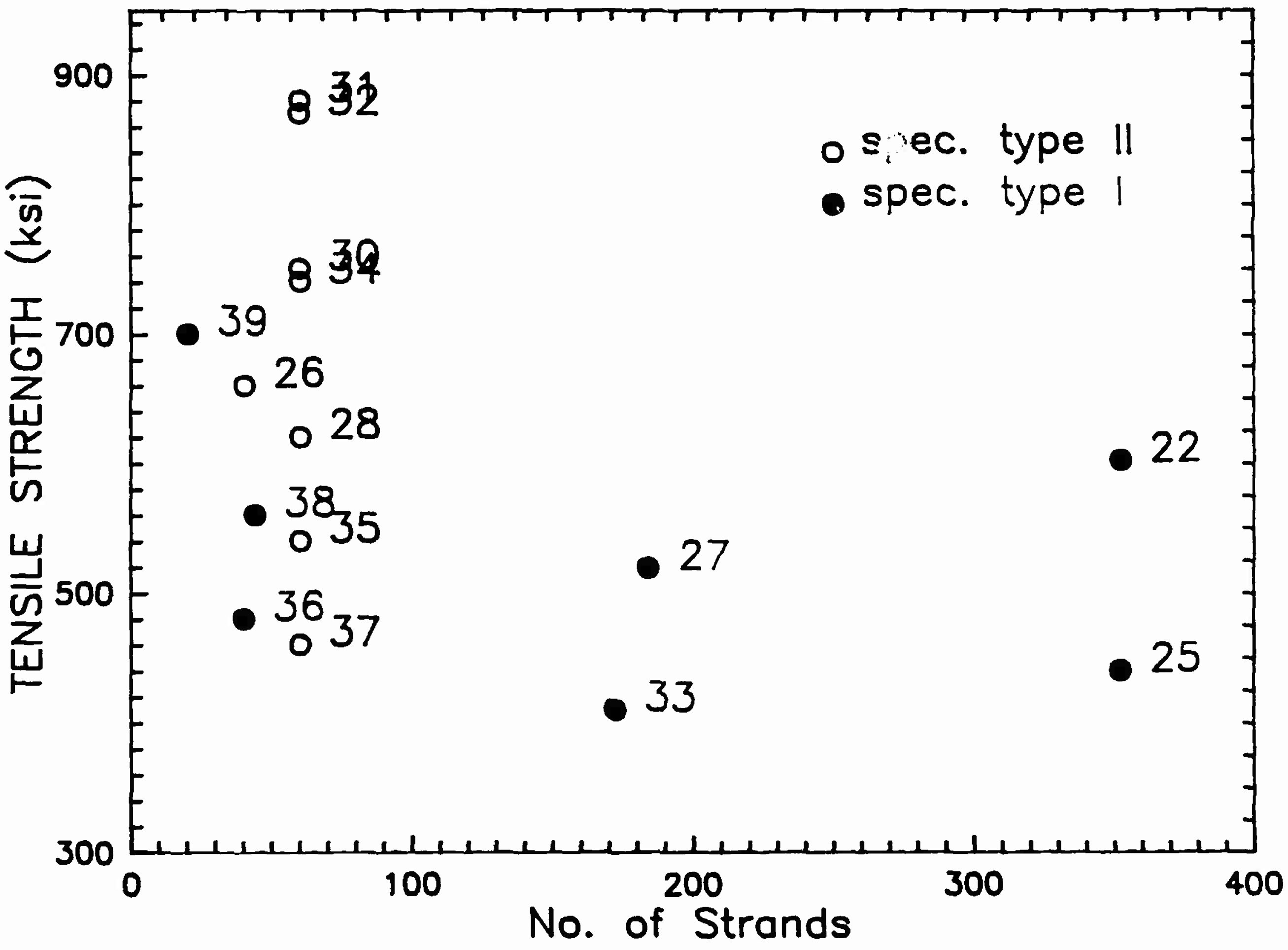

Figure 3.7. Strength of S-2 Glass® bundles from split Hopkinson bar testing.

SECTION 4

REFERENCES

1. S. J. Bless and D. R. Hartman, "Ballistic Penetration of S-2 Glass® Laminates," Proceedings 21st SAMPE Conference, Atlantic City, New Jersey, 1989.

2. M. Benyami, S.J. Bless, and D. L. Jurick, "Techniques to Study Penetration Through Glass Reinforced Phenolics," Presented at the Aeroballistic Range Association Meeting, San Diego, CA, October 1990.

3. A. Vasudev, K. Okajima, and S.J. Bless, "Effects of the Transverse Strength and the Density on the Penetration of Thick Glass-Fiber-Reinforced Plastics," 10th Int. Symposium on Ballistics, San Diego, CA, October 1987.

4. K. Saka and J. Harding, "Behavior of Fiber-Reinforced Composites Under Dynamic Tension," Interim Report, AFOSR-TR-87-0819, Bolling AFB, October 1986.

5. A. E. Armenakas, et al., "Experimental Study of the Failure Mechanism and Strength Characteristics of Fiber Bundles and Composites," J. Experimental Mechanics, January 1972.

6. S. W. Tsai and S. Schulman, "A Statistical Analysis of Bundle Tests," Air Force Materials Laboratory Technical Report AFML-TR-67-351, Wright-Patterson Air Force Base, Dayton, OH, April 1968.

7. S. V. Serensen and V. S. Strelyaev, "Progressive Failure of Groups (Bundles) of Reinforcing Fibers of Varying Strengths," Moscow Aviation Technological Institute, Translated from Problemy Prochnosti, 10, 3-8 (1970).

8. A. E. Armenakas, S. K. Garg, and C. A. Sciammarella, "Strength Characteristics of Glass Fibers Under Dynamic Loading," J. Appl. Phys., 41, 4, 1657 (1970).

9. Private communication with Mr. D. Hartman, Owens/Corning Fiberglas Co.

10. T. Nicholas, Exp. Mech., 21, 177 (1980).

11. J. Cagnoux, "Deformation and Failure of Glass Pyrex Subjected to Intense Shock; Experimental Study and Behavior Modeling," Ph.D. Thesis, Universite De Poitiers, May 24, 1985.

12. S. Bless and D. Hartman, K. Okajima, and S. Hanchak, "Ballistic Penetration of S-2 Glass® Laminates", S-2 Glass® Fiber Technical Paper, Owens/Corning Fiberglas Co. Pub. No. 4-ASP-14493, March 1987.

13. R. H. Zee, B. Z. Jang, A. Mount, and C. J. Wang, Rev. Sci. Instrum., 60 (12), 3692 (1989).

14. C. Y. Hsieh, et. al., 22nd Int. SAMPE Technical Conference, November 6-8, 1990.

15. R. L. Woodward and I. G. Crouch, Proceedings 11th Int. Symp. on Ballistics, Brussels, Belgium, Royal Academy, Vol. II, 301 (1989).

16. G. T. Egglestone, E. P. Gellert, and R. L. Woodward, Conference Proceedings Materials United in The Service of Man, Perth, Western Australia, September 17-21, 1990. Ed. R. D. Davies and D. I. Hatcher.

17. S. J. Bless, M. Benyami, and D. R. Hartman, 22nd Int. SAMPE Technical Conference, November 6-8, 1990.

18. S. J. Bless, D. R. Hartman, and S. J. Hanchak, Symposium on Composite Materials in Armament Applications, U. S. Army Armament R&D Center, Picatinny Arsenal, Dover, NJ, August 20-22, 1985.

19. S. Bless, S. Hanchak, K. Okajima, and D. Hartman, "Ballistic Penetration of S-2 Glass Laminates," Third TACOM Armor Coordinating Conference, Monterey, CA, February 17-19, 1987.

20. S. Bless, M. Benyami, and D. Hartman, "Penetration Through Glass-Reinforced Phenolic," 22nd SAMPE Technical Conference Proceedings, Boston, MA, November 1990.

21. S.J. Bless and D.R. Hartman, "Ballistic Penetration of S-2 Glass Laminates," Proceedings 21 SAMPE Conference, Atlantic City, NJ, September 1989.

22. M. Benyami, S.J. Bless, and D.L. Jurick, "Techniques to Study Penetration Through Glass Reinforced Phenolic," Aeroballistic Range Association, October 1990.

23. M.J. Forrestal, V.K. Luk, and N.S. Brar, "Performation of Aluminum Armor Plates With Conical-Nose Projectiles," Mech. of Matls. 10, 97-105 (1990).

24. W. Walters, Private communication, 1990.

25. Z. Rosenberg, D. Yaziv, and S. Bless, "Spall Strength of Shock Loaded Glass," J. Appl. Phys., 58, 3249 (1985).

26. Z. Rosenberg and M. Forrestal, "Perforation of Aluminum Plates With Conical-Nosed Rods--Additional Data and Discussion," J. Mech. Phys. 236-238 (1988).

27. R. Hill, Mathematical Theory of Plasticity, Oxford, London, 1950.

28. S. Jeng and J. Fan, "Transient Response of Pultruded Fiber Reinforced Plastic Rod Subject to Impact Loading," 35th International SAMPE Symposium, April 2-5, 1990.

29. L. Welsh and J. Harding, "Dynamic Tensile Response of Unidirectionally-Reinforced Carbon Epoxy and Glass Epoxy Composites," Report No. OUEL 1579/85, University of Oxford, UK.